



## Study of a building integrated bifacial photovoltaic facade

Ya Brigitte Assoa<sup>a,\*</sup>, Philippe Thony<sup>a</sup>, Paul Messaoudi<sup>a</sup>, Emmanuel Schmitt<sup>b</sup>, Olivier Bizzini<sup>c</sup>,  
Stephane Gelibert<sup>c</sup>, Didier Therme<sup>a</sup>, Julie Rudy<sup>a</sup>, Fabien Chabuel<sup>a</sup>

<sup>a</sup> Univ. Grenoble Alpes, CEA, LITEN, DTS, LAM, F-38000 Grenoble, France

<sup>b</sup> VICAT, 4 Rue Aristide Berges, 38081 L'Isle-d'Abeau, France

<sup>c</sup> ARAYMOND France, 1 Rue Louis Besançon, 38120 Saint-Egrève, France

### ARTICLE INFO

#### Keywords:

Building Integrated Photovoltaic (BIPV)  
Bifacial PV modules, experimentation  
Building total energy performance  
Concrete facade

### ABSTRACT

An increase of knowledge of the mid-term performance of building integrated bifacial photovoltaic modules in real conditions is required in order to validate their relevance. Thus, in this work, the experimental study during more than one year of an innovative building integrated bifacial photovoltaic ventilated facade developed in the framework of the CONIPHER Life project and mounted on a test cell at Le Bourget du Lac is presented focusing mainly on the photovoltaic modules thermal behaviour and electrical performance. Moreover, a specific attention is made on the photovoltaic facade seasonal impact on the building energy consumption compared to a similar test cell comprising a non-insulated concrete wall. An important thermal gradient is observed along the facade in warm season, as expected, mainly due to site albedo, with mean photovoltaic modules temperature up to 68.3 °C. The innovative facade produced an annual cumulated electrical energy of 63.8 kWh/m<sup>2</sup> with a performance ratio of 0.7 and a mean annual efficiency of 6.3%. A huge reduction of the building total energy consumption up to 92% in winter compared to reference is observed. As further studies, the facade will be installed on an office building in order to demonstrate its performance in real conditions.

### 1. Introduction

Considering its whole life cycle, building sector is responsible for 40% of total European energy consumption and 36% of greenhouse gas emissions. The renovation of 3% of existing buildings is, thus, encouraged. In this sense, in accordance with the European energy policies of 2010, the construction of Nearly Zero-Energy Buildings integrating renewable energy sources such as solar photovoltaics is essential for a total or major coverage of energy needs (EU, 2020). Indeed, the building envelope is a critical element since it influences the indoor thermal loads but it also represents a large available area for energy production, especially facades.

However, in the case of facade integrated photovoltaic installations, a decrease of electrical performance is observed compared to rack-mounted or rooftop photovoltaic systems mainly due to the higher risk of shading and to the less advantageous solar incident angle (Vulkan et al., 2018) in addition to the expected modules overheating and the important thermal gradient from top to bottom of the facade (Freitas and Brito, 2019). Moreover, in urban area, these more visible systems have to comply with the public, market, architects and regulatory

requirements concerning aesthetics and performance more than rooftop installations (Attoye et al., 2017), thus the development of innovative and aesthetical photovoltaic prototypes for facade integration with improved performance is necessary, especially for building deep renovation (Saretta et al., 2019; Shukla et al., 2017; Freitas and Brito, 2019). Various configurations of building integrated facades can be found in the literature including different photovoltaic modules technologies (opaque or semi-transparent, crystalline silicon or thin film) but, only few projects include bifacial photovoltaic modules although the additional electricity production at their backside (Gu et al., 2020), leading to the lack of knowledge on their performance in real conditions and so, to the slow development of their application in the building sector. Thus, numerical and experimental studies in situ and on at least one year are necessary to validate the relevance of this technology for a building integration.

According to the state of art, photovoltaic modules are applied in four main kinds of facade elements, namely, solar glazed facades, sun-shading elements, ventilated facades (with an air gap at the rear side of photovoltaic modules) and non-ventilated facades (photovoltaic modules directly in contact with the facade). For a satisfactory rear side production, the use of bifacial photovoltaic modules requires the

\* Corresponding author.

E-mail address: [ya-brigitte.assoa@cea.fr](mailto:ya-brigitte.assoa@cea.fr) (Y.B. Assoa).

<https://doi.org/10.1016/j.solener.2021.09.004>

Received 22 April 2021; Received in revised form 31 August 2021; Accepted 3 September 2021

Available online 20 September 2021

0038-092X/© 2021 International Solar Energy Society. Published by Elsevier Ltd. All rights reserved.

Nomenclature	
<i>Symbols</i>	
AC	Alternative current
BIPV	Building integrated photovoltaic module
C <sub>p</sub>	Electrical performance loss coefficient (-)
dT <sub>j</sub>	Absolute difference of temperatures of layer j (°C)
E <sub>ac</sub>	Electrical energy produced in AC (Wh)
E <sub>i</sub>	Incident solar energy (Wh/m <sup>2</sup> )
E <sub>pvmf</sub>	Electrical energy production of the monofacial PV modules (Wh)
EVA	Ethylene vinyl acetate
G <sub>i</sub>	Incident total solar radiation (W/m <sup>2</sup> )
G <sub>STC</sub>	Incident solar radiation in standard tests conditions (STC)
HET	Heterojunction photovoltaic module
I <sub>sc</sub>	Short circuit current (A)
NOCT	Nominal operating cell temperature conditions
P <sub>max</sub>	Nominal power installed (Wp)
P <sub>pvmf</sub>	Electrical power production of the monofacial PV modules (W)
Prac	Performance ratio after inverter (-)
PV	Photovoltaic module
Spv	Surface of the PV field (m <sup>2</sup> )
STC	Standard tests conditions
T <sub>i</sub>	Temperature of i material (°C)
V <sub>oc</sub>	Open-circuit voltage (V)
Y <sub>f</sub>	Final yield (kWh/kWp)
<i>Greek</i>	
η <sub>pv</sub>	Electrical efficiency of the photovoltaic module (%)
<i>Subscripts</i>	
mean	Mean value
PV, pv1	Photovoltaic
pv3	Photovoltaic module 3
pv5	Photovoltaic module 5
ref	Reference value
STC	Standard tests conditions

installation of a reflective layer located at an optimal distance and reflecting solar radiation towards their backside (Chen et al., 2021; Soria et al., 2015; Ko et al., 2021; Kim et al., 2021; Muehleisen et al., 2021), which is mainly possible with ventilated façades. Nevertheless, for an integration into non-ventilated facades, since the bifacial photovoltaic modules have a semi-transparent structure, the reflective layer could be mounted directly in contact with their rear glass in order to exploit its optical properties (reflection coefficient of the glass layer). Moreover, the reflection properties of the coating of a room internal walls (ceiling, walls and floor) could be adapted in the case of solar glazed facades (Chen et al., 2021).

Only few research studies on photovoltaic facades including bifacial technologies could be found in literature. In 2015, Soria et al. analysed numerically and experimentally on short periods the relevance of the integration of a semi-transparent bifacial technology to a ventilated facade from the electrical and optical points of view and considering various innovative module architectures, air gap thicknesses and reflective layer materials. They obtained numerically an annual electrical energy gain of nearly 25% on a small scale test bench compared to a standard photovoltaic module (Soria et al., 2015). Then, in 2020, Tina et al. compared numerically the daily thermal behaviour and electrical performance of four non-insulated building integrated photovoltaic facades and their heat exchange with the building envelope. The systems considered in their study were differentiated by the presence of an air gap, by the reflective surface material (standard wall plaster or highly reflective paint with reflective coefficients of, respectively 0.2 and 0.7) and by the photovoltaic technology (standard or bifacial modules). They explained that the use of bifacial modules, even with the plaster coating as reflective layer, permitted an increase of the electrical power produced in peak hours of 2.9% compared to the monofacial photovoltaic ventilated façade and of 4.4% compared to the non-ventilated one. Moreover, the use of the reflective paint led to an additional increase of production of nearly 2.9% (Tina et al., 2020).

These studies present interesting parametric studies permitting to estimate the impact of the bifacial system operating conditions on its performance. Nevertheless, experimental studies are realized on reduced scale facade installations, on short periods (hours, days, weeks, months) and annual data are obtained only through simulation, which is not sufficient to validate the relevance of this technology especially with industrial and financing partners. (Tina et al., 2020; Soria et al., 2015; Chen et al., 2021)

In this sense, in this work, the experimental study of an innovative configuration of building integrated glass-glass bifacial photovoltaic

ventilated facade is presented focusing mainly on the thermal behaviour and the electrical performance of the photovoltaic modules, which has not been proposed previously on an annual base and at full scale. In addition, a specific attention is made on the whole facade solution comprising the bifacial photovoltaic modules, their rear side reflective concrete panels and the facade insulation layer through the evaluation of its seasonal contribution to reduce a building total energy consumption compared to a standard non-insulated concrete wall. Indeed, the various studies existing on this aspect highlight that a ventilated photovoltaic facade configuration contributes to reduce the cooling load in summer while a non-ventilated system has a positive impact on heating load in winter, when it is well designed (Yu et al., 2021; Tina et al., 2020; Li et al., 2019; Han et al., 2019; Wang et al., 2017). More precisely, Peng et al. showed numerically that compared to a standard concrete wall, a solar double skin photovoltaic wall could permit a reduction of heat gain by 51% in summer and of heat loss by 32% in winter (Peng et al., 2013). Then, in 2019, Li et al. modelled and tested a non-ventilated precast concrete photovoltaic facade for high-rise buildings permitting a heating load saving of 19.67 kWh/m<sup>2</sup>/year (corresponding to a relative difference of nearly 56.7%) and an increase of cooling load of 14.70 kWh/m<sup>2</sup>/year compared to a concrete wall (Li et al., 2019).

In this paper, the design of the innovative bifacial photovoltaic facade element is first presented. Then, the outdoor tests performed on two full scale test cells at Le Bourget du Lac integrating the south-oriented facade studied and a reference non-insulated concrete wall in order to measure thermal, electrical, energy consumption and weather data during more than one year are described. The temperature and electrical production of the photovoltaic modules are analysed on daily, monthly and annual bases. Moreover, in order to estimate the impact of the system on heat transfers through the integration facade, the temperature distributions along the two facades are compared using thermal images. Finally, a comparison of the tests cells total energy consumption for heating and cooling is proposed considering the cold and the warm periods.

## 2. Description of the BIPV facade element designed

The innovative bifacial photovoltaic (PV) facade element studied was designed in the framework of the CONIPHER Life project mainly in order to encourage deep energy renovation of building facades. Its configuration aims mainly to ensure a reduction of energy consumption for heating of at least 60% compared to standard non-insulated concrete

wall through a sealed fastening solution for an easy and fast installation and dismantling of the bifacial PV modules and a whole facade high thermal resistance of nearly  $5 \text{ m}^2 \cdot \text{K}/\text{W}$ .

The prototype configuration was thus developed in order to solve some expected issues such as the thermal bridges within the insulation layer due to fastening nuts and the reduced level of cooling of building integrated PV modules backside.

The photovoltaic facade basic element of 0.9 m long and 0.83 m wide is composed of a nearly 57 Wp bifacial glass-glass photovoltaic module (see Fig. 1a and b) comprising a 2 cm thick fully open air gap and an insulated ultra-high performance fiber concrete panel of Vicat company at the rear side. It is fixed on the initial concrete wall of the test cell using four fastening nuts (see Fig. 2a–c). The fastening profiles combined with thermal breaking plastic caps and expansion joints were specifically designed by ARaymond company for the project considering also seismic risks (see Fig. 2a and b).

Eight PV basic elements were mounted in an open joint ventilated facade configuration (Agathokleous and Kalogirou, 2016; Sanjuan et al., 2011a) leading to air entering or exiting the discontinuous air gap at different levels between the PV modules. According to the BIPV facade layout (in two columns of four PV modules), outdoor air will tend to enter in the air gap at the bottom and the top of the first row of PV modules and to exit at the bottom and top of the upper row of PV modules (see Fig. 2c).

The eight integrated octagonal semi-transparent bifacial PV modules were manufactured by CEA. Each module of 0.854 m long and 0.763 m wide (with a  $45^\circ$  chamfer of glass layers reducing the PV module length and width of 81 mm) is composed of a 3 mm thick tempered front glass, a  $600 \mu\text{m}$  ethylene vinyl acetate (EVA) front layer, 24 monocrystalline silicon heterojunction (HET) bifacial half-cells in series (set out in 6 columns and 4 rows), a  $600 \mu\text{m}$  EVA back layer and a 3 mm thick tempered back glass. The transparency rate of each PV module was of nearly 61.6%. The half-cells were obtained by cutting  $15.6 \text{ cm} \times 15.6 \text{ cm}$  PV cells with a method patented by CEA (CEA, 2018). The weight of the PV module is of nearly 10.2 kg. The use of half-cells permitted to increase the PV module voltage without modifying its size for a compatibility with standard inverter technologies (Soria et al., 2015) (see Fig. 1).

Since the reflective coefficient values of a concrete material are comprised between nearly 0.25 and 0.30 over the visible spectrum (from 380 nm to 780 nm) (Jensen, 2007; Raybaud et al., 2019), the smooth surface of the 2 cm thick fiber concrete panels was used as reflective layer without specific treatment, as first hypothesis. Fig. 2c summarizes the working principle of the solar bifacial facade studied including the expected air flow direction in the air gap and the main solar radiation transmission through its different layers. More precisely, the solar radiation that reaches directly the front side of PV cells is partly absorbed

(by the front glass layer on the corresponding areas and the PV cells) and partly reflected towards environment. The solar radiation reaching the semi-transparent areas of PV modules is partly reflected, absorbed and transferred by their glass layers. The transferred part of the solar radiation is partly absorbed by the insulated fiber concrete panels and reflected towards the rear face of PV modules (and thus, of PV cells) for an additional electrical power production. The solar radiation reaching directly the fiber concrete panels and their interfaces is partly absorbed and partly reflected towards the rear face of PV cells and environment (see Fig. 2c). It is to be noted that existing multiple absorption, transmission and reflection of solar radiation in the air gap and within the PV modules are not represented in Fig. 2c.

Finally, for the choice of the insulation layer material, in order to reach the expected facade thermal properties, a comparison of different insulation products (phenolic foam, glass fiber wool, rock wool and foamed glass) was performed considering their environmental impact, their physical properties and their costs. Table 1 presents the main results obtained based on the insulation materials environmental product declarations (EPD, 2021) and considering  $1 \text{ m}^2$  of panel with a facade thermal resistance of  $5 \text{ m}^2 \cdot \text{K}/\text{W}$  (value defined based on requirements for facades of the French thermal regulation RT2012) (ADEME, 2021).

The phenolic foam has the lowest thermal conductivity (of  $0.021 \text{ W}/\text{m K}$ ) permitting to obtain the required thermal resistance with a reduced thickness compared to other insulation materials. Moreover, for  $1 \text{ m}^2$  of insulation layer, the phenolic foam panel is the lightest (with 3.5 kg) but is more expensive (with 55 Euros/ $\text{m}^2$ ) than the rock wool panel and the glass wool panel (with respectively, 22 Euros/ $\text{m}^2$  and 20 Euros/ $\text{m}^2$ ). The glass wool panel seems competitive because of its low weight (of 4.32 kg) and cost, but its reduced rigidity (density of  $27 \text{ kg}/\text{m}^3$ ) increases risks of packing and thus, risks of early degradation of the complete solar element. The rock wool panel has a limited weight (of 11.55 kg) and is more rigid than glass wool panel (with a density of  $70 \text{ kg}/\text{m}^3$ ) to limit risks of packing. The foamed glass is the densest (with  $120 \text{ kg}/\text{m}^3$ ) but it is the heaviest (with 24 kg) and the most expensive (with 240 Euros/ $\text{m}^2$ ). Moreover, its energetic footprint is in most cases, the highest, taking into account environmental impact (for example, with 32.4 kg CO<sub>2</sub>-eq. of global warming potential), waste generation (with 25.2 kg of non-hazardous waste disposed) and resource use (with 497.7 MJ of total use of non-renewable primary energy resources) (see Table 1).

With a high fire resistance, a sufficient density and a competitive cost, a 20 cm thick rock wool insulation layer (of  $0.033 \text{ W}/\text{m K}$  of thermal conductivity) was selected as a good compromise for the studied prototype. Moreover, it is fully recyclable and has a reduced energy footprint compared to the other insulation materials considered, with 13.2 kg CO<sub>2</sub>-eq. of global warming potential, 0.107 kg SO<sub>2</sub>-eq. of acidification potential of land and water, 0.00751 kg (PO<sub>4</sub>)<sub>3</sub>-eq. of eutrophication potential, 0.00619 kg C<sub>2</sub>H<sub>4</sub>-eq. of formation potential of

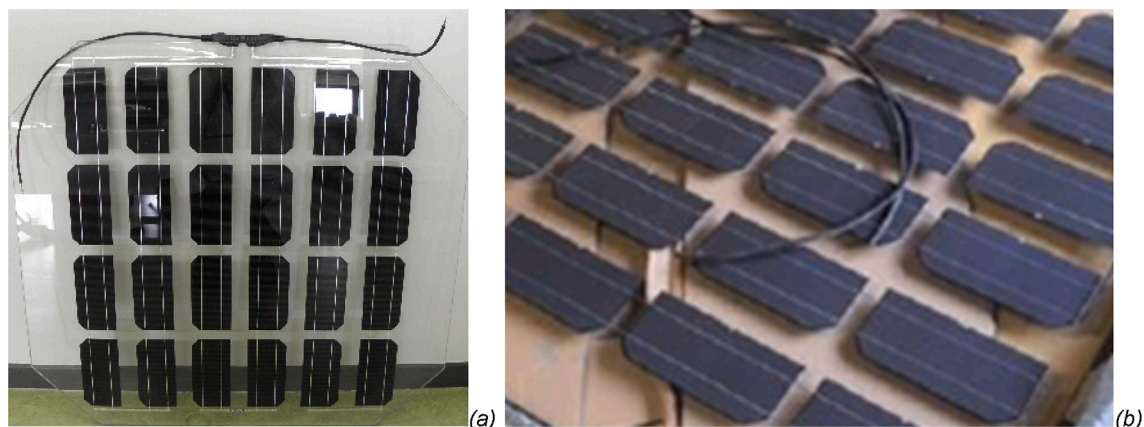
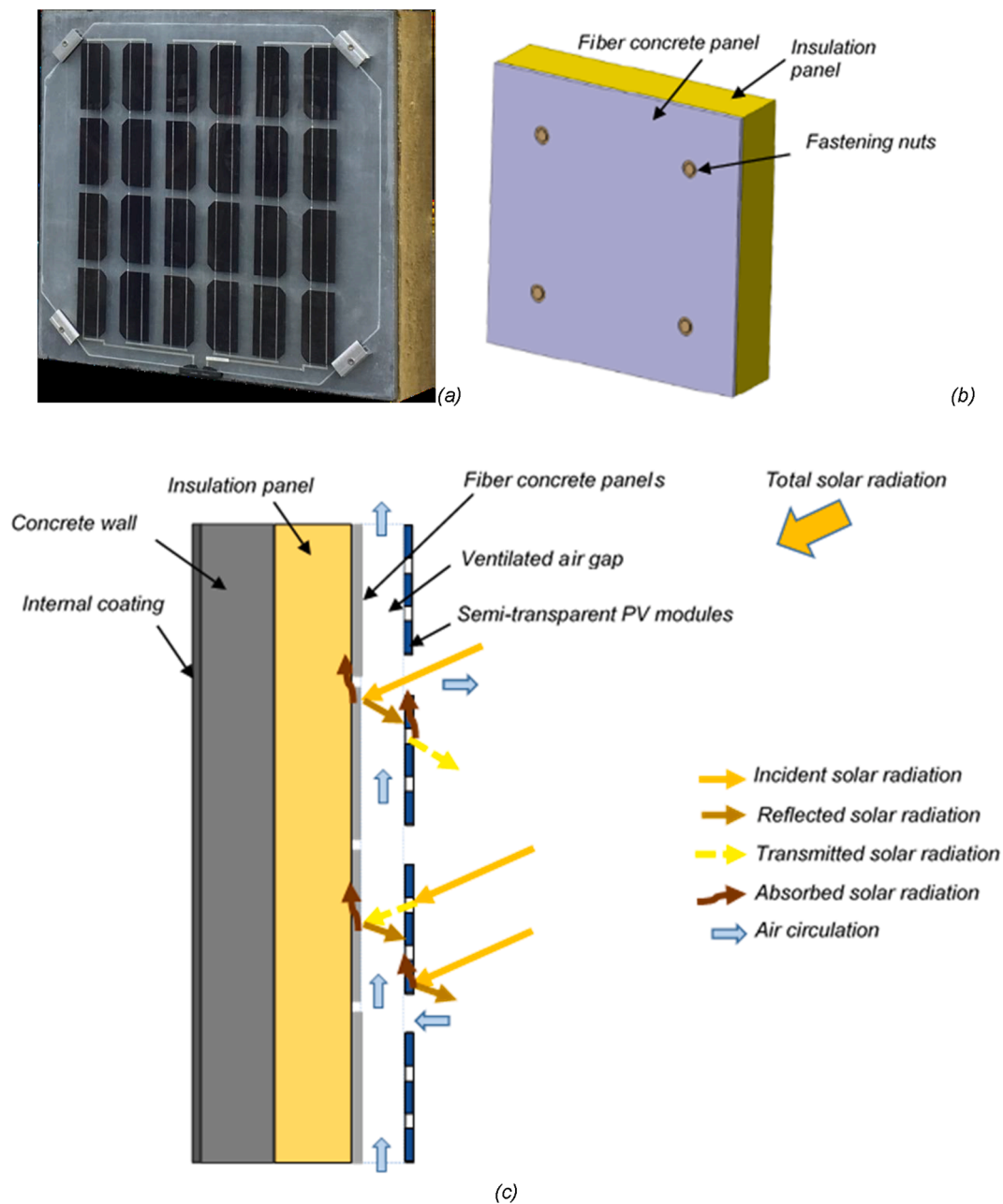


Fig. 1. CONIPHER Heterojunction bifacial photovoltaic module (a: front side; b: backside).



**Fig. 2.** Schemes of the insulated fiber concrete panel (a) and photograph (b) of the CONIPHER BIPV panel and working principle on the solar facade vertical section considering expected air flow direction in the air gap and main solar radiation transmissions (with PV cells on blue zones and semi-transparent areas on white zones of PV modules) (c).

tropospheric ozone photochemical oxidants, 0.000000536 kg Sb-eq of abiotic depletion potential for non-fossil resources, 10.7 MJ of total use of renewable primary energy resources, 174.9 MJ of total use of non-renewable primary energy resources, 14 kg of non-hazardous waste disposed and 0.000446 kg of radioactive waste disposed (see Table 1).

Prior to the tests campaign, flash-tests and electroluminescence tests have been performed on the eight PV modules under standard test conditions (or STC, corresponding to a solar radiation of  $1000 \text{ W/m}^2$ , a PV cell temperature of  $25 \text{ }^\circ\text{C}$  and an air mass of 1.5) considering only their front side in order to obtain their electrical characteristics (see Table 2 and Fig. 3a), although the bifaciality.

Table 2 shows that the eight selected bifacial PV modules have a mean power output of nearly  $57 \text{ Wp}$  with less than 1% of variance. Their mean electrical open-circuit voltage and mean short-circuit current are respectively of nearly  $17 \text{ V}$  and  $4.6 \text{ A}$ , with a mean cell efficiency of

nearly 20%. The PV modules efficiency is of nearly 8.7%.

Fig. 3 presents an example of electroluminescence image of a bifacial PV module showing no sign of cells crack.

Then, the thermal behavior and electrical performance of the developed photovoltaic system was evaluated experimentally in situ during nearly one year.

### 3. Description of the experimental setup

The innovative system was integrated on the south-oriented facade of a test cell of the FACT facility (FACade Tool) at CEA site and instrumented. A test campaign was performed from December 2018 to December 2019 in order to estimate the thermal behavior and the electrical production of the photovoltaic facade and the test cell energy consumption for heating and cooling. A concrete wall was also mounted

**Table 1**

Comparison of physical properties, costs and environmental impacts (based on their environmental product declarations) of 1 m<sup>2</sup> of the insulation products considered (phenolic foam, glass fiber wool, rock wool and foamed glass) providing a facade thermal resistance of 5 m<sup>2</sup>.K/W:

	Phenolic foam	Rock Wool	Foamed Glass	Glass wool
Cost (Euros/m <sup>2</sup> )	55	22	240	20
Weight (kg)	3.50	11.55	24	4.32
Density (kg/m <sup>3</sup> )	35	70	120	27
Thickness (cm)	10	16.5	20	16
Thermal conductivity (W/m.K)	0.021	0.033	0.040	0.032
Lifetime (year)	50	50	50	50
<b>Environmental impact</b>				
Global warming potential (kg CO <sub>2</sub> -eq)	9.9	13.2	32.4	5.12
Acidification potential of land and water (kg SO <sub>2</sub> -eq)	0.024	0.107	0.072	0.0304
Eutrophication potential (kg (PO <sub>4</sub> ) <sub>3</sub> -eq)	0.00497	0.00751	0.00904	0.00480
Formation potential of tropospheric ozone photochemical oxidants (kg C <sub>2</sub> H <sub>4</sub> -eq)	0.00990	0.00619	0.00481	0.00448
Abiotic depletion potential for non-fossil resources (kg Sb-eq)	0.0000185	0.00000536	0.000169	0.00000176
<b>Resource use</b>				
Total use of renewable primary energy resources (MJ)	4.2	10.7	216.2	13.0
Total use of non-renewable primary energy resources (MJ)	292.4	174.9	497.7	144.0
<b>Waste</b>				
Non-hazardous waste disposed (kg)	5.1	14.0	25.2	6.4
Radioactive waste disposed (kg)	0.00171	0.000446	0.00537	0.000544

**Table 2**

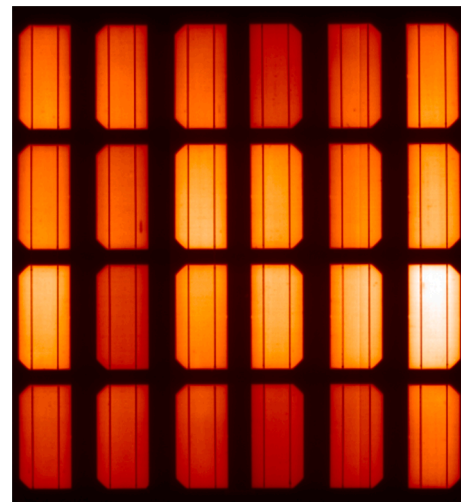
Electrical characteristics of the eight bifacial PV modules measured with flash-tests: minimum, maximum and mean values of results obtained.

Characteristics	Summary of performance measured			
	Mean	Max	Min	Variance
Open circuit voltage Voc (V)	17.02	17.17	16.91	0.42%
Short-circuit current Isc (A)	4.60	4.65	4.55	0.63%
Nominal electrical power Pmax (Wp)	57.41	58.28	56.71	0.88%
Cell efficiency (%)	20.02	20.32	19.78	0.88%
Fill Factor (%)	73.29	74.80	72.48	0.98%

and instrumented on a similar test cell used as reference.

### 3.1. Presentation of the test cells instrumentation

FACT tool is located at CEA site at Le Bourget du Lac (45°38'44"N, 5°51'33"E) and is a two-storey modular test building dedicated to envelope components tests and comprising ten cells (of 2.3 m of width, 3.9 m of length and 3.3 m of height) (see Fig. 3a). The installation site climate is characterized by warm and dry summers and mild winters

**Fig. 3.** Electroluminescence image of a bifacial PV module.

with monthly mean ambient temperatures comprised between 1.6 °C in January and 20.4 °C in July.

Fig. 4b presents a photograph of the south-oriented facades of the two test cells considered for this study and which are 2.3 m wide and 3.3 m high. On the right side of Fig. 4b, the 20 cm thick non-insulated cast concrete façade of a test cell (noted test cell 4) comprised the eight bifacial photovoltaic basic elements connected in series to an Enphase M215 micro-inverter located in the room. On the left side, the second test cell (noted test cell 3) was used as reference and comprised a 20 cm thick non-insulated cast concrete wall. A similar internal plaster coating was added on both facades. All other facades of the two test cells were highly insulated in order to reduce solar gains and heat transfers with environment (with outdoor ambient air temperature and sky temperature) and with adjacent cells (see Fig. 5a).

The indoor air setpoint temperature in the two tests cell was fixed with a CLIMACIAT AIRTECH 25 dual-flow air handling unit from CIAT at nearly 21 °C in cold season and at nearly 26 °C in warm season (see Fig. 5b).

A suitable similar instrumentation was defined for the two test cells for comparison, in order to obtain weather, thermal, electrical and energy consumption data (see Figs. 6 and 7).

More precisely, in the test cell 4, T-type thermocouples were stuck with aluminum tapes at various locations of the wall: on the PV modules 3 and 5 front glass layer avoiding shadings on PV cells, at the interfaces of the facade layers at the level of each PV module, on the internal coating at the level of each PV module and of the interfaces between PV modules 3 and 5 and PV modules 4 and 6 in order to identify possible thermal bridges and then, on the fiber concrete panels of the PV modules 3, 4, 5 and 6 (see Fig. 6a–c). It is to be noted that for technical constraints related to thermocouples cables passage at the interface around the concrete wall, the number of sensors to be installed directly on the PV modules had to be limited. Thus, supposing the studied system vertical symmetry and the air flow distribution in an open joint ventilated façade (flow entering at the top and the bottom of the lower PV modules and leaving the air gap at the top and the bottom of the upper ones (Sanjuan et al., 2011a)) (see Fig. 2c), only half of the south-oriented PV field was instrumented and more precisely, the PV modules close to its center (PV module 3 and PV module 5, here), in order to obtain a relevant mean system temperature.

In the test cell 3, thermocouples were stuck on both sides of the cast concrete wall at the right side (see Fig. 6d).

In both test cells, a T-type thermocouple and a flux meter (Hukseflux of Campbell scientific) were stuck on each wall. Two additional flux meters were mounted on the internal coating of the test cell 4 at the level of PV modules 3 and of its interface with PV module 4 (area without PV



Fig. 4. Photographs of FACT tool (a), of the south-oriented reference wall (on the left side) and of CONIPHER project BIPV wall (on the right side) (b) at CEA site (at Le Bourget du Lac).

module) (see Figs. 6a and 7). A flux meter was also added at the interface between the insulation layer and the concrete wall at the level of PV module 3 in order to analyze more precisely the heat flux distribution within the facade (see Fig. 6b).

Moreover, a thermal camera was used to observe temperature distribution on the two facades. Measurements of indoor ambient air temperature were realized with thermocouples located at 1 m, 2 m and 3 m from the floor level. An anemometer (of Delta Ohms) permitted to measure air velocity in each test cell and, in order to reduce stratification, a fan was activated to mix air.

Electrical values (power, voltage and current) after inverter were provided by the micro-inverter connected to a communication gateway using an in-house monitoring program developed in Labview NI software.

A weather station existing on CEA site closed to FACT tool permitted to obtain the outdoor ambient air temperature with a sheltered PT100 sensor, the total horizontal solar radiation with a pyranometer in the horizontal plane and the wind velocity and direction with a Windsonic anemometer. An additional pyranometer on the south-oriented facade of FACT tool provided the total solar radiation in the vertical plane (in the PV modules plane).

Two thermal energy meters were used to measure the thermal power (with positive values corresponding to heating periods) permitting then, to calculate the energy consumption for heating and cooling in the two test cells (by numerical integration on a defined period of the thermal power measured on each time step in hour).

All sensors were connected to a local Agilent datalogger and measured data with a 1 min time step were stored on a CEA common database. Uncertainties of sensors are presented in Table 3.

### 3.2. Parameters considered for the analysis of the BIPV system electrical performance

Three main parameters were used for the analysis of the measured electrical data, namely, the performance ratio after the micro-inverter  $Prac$  (-), the electrical efficiency  $\eta_{pv}$  (-) and the final yield  $Y_f$  (kWh/kWp), which are provided respectively by Eqs. (1)–(3). The performance ratio permits to evaluate the energy production of the system compared to STC conditions (corresponding to a  $Prac$  value of 1). More precisely, the performance ratio permits to take into account the impact of various operating conditions parameters (such as inverter issues, shading, wiring losses, cell mismatch, modules temperature or outages) on the PV system electrical energy production (Khalid et al., 2016; Assoa et al., 2017; Cubukcu and Gumus, 2020).

The electrical efficiency is the ratio between the electrical energy produced and the solar energy received by the PV system area.

The final yield  $Y_f$  is the ratio between the electrical energy produced and the nominal power installed and permits to evaluate the number of times the PV system has produced an electrical energy equal to its nominal power on a defined period.

$$Pr_{ac} = (E_{ac}/P_{max})/(E_i/G_{STC}) \quad (1)$$

$$\eta_{pv} = E_{ac}/(E_i \cdot S_{pv}) \quad (2)$$

$$Y_f = E_{ac}/P_{max} \quad (3)$$

With  $E_{ac}$ , the electrical energy produced in AC (kWh) that is the numerical integration of the measured electrical power produced by the PV field on a defined period (time step in hour),  $E_i$  the cumulated incident solar energy (kWh/m<sup>2</sup>) obtained with the numerical integration of the measured incident total solar radiation received at the front side of the PV modules on the same period (time step in hour),  $G_{STC}$  the incident solar radiation in standard tests conditions (STC) (equal to 1 kW/m<sup>2</sup>),  $P_{max}$  the nominal power (kWp) of the PV modules front side obtained with flash-tests (see Table 2) and  $S_{pv}$  the PV field area including, here, only the PV modules front glass areas (m<sup>2</sup>).

Moreover, in order to evaluate the impact of bifaciality on the BIPV field electrical performance, Eq. (4) was used to calculate an electrical power (noted  $P_{pvmf}$ ) produced by a PV field comprising monofacial PV modules with electrical characteristics similar to the ones of the studied bifacial PV modules front side (see Eq. (4)) (Kaldellis et al., 2014). A theoretical electrical efficiency  $\eta_{pv1}$  was estimated, in this case, based on  $T_{pvmean}$ , the bifacial PV field measured mean temperature (corresponding to an average of the PV module 3 and the PV module 5 measured temperatures) and neglecting the difference of temperatures between the bifacial and the monofacial PV modules (Chow, 2003) (see Eq. (5)):

$$P_{pvmf} = \eta_{pv1} \cdot G_i \cdot S_{pv} \cdot C_p \quad (4)$$

$$\eta_{pv1} = \eta_{ref} \cdot (1 - \beta_r \cdot (T_{pvmean} - T_{pvref})) \quad (5)$$

With  $\eta_{ref}$  and  $SPV$  respectively, the reference PV modules efficiency (of 8.7% in STC, here) and the PV modules area (m<sup>2</sup>).  $G_i$  is the incident total solar radiation (W/m<sup>2</sup>) and  $\beta_r$  is the temperature coefficient (supposed equal to  $-0.37\%/^{\circ}\text{C}$ , for a monocrystalline silicone PV module).  $T_{pvref}$  is the reference PV module temperature (of 25 °C, in STC).

Then, a performance loss coefficient  $C_p$  was considered and supposed to be equal to 0.62 (mean value used at standard test conditions (STC)) in order to take into account losses due to grid-integration (conversion from DC to AC power, DC and AC electrical systems, inverter losses, etc.). (Marion et al., 2005)

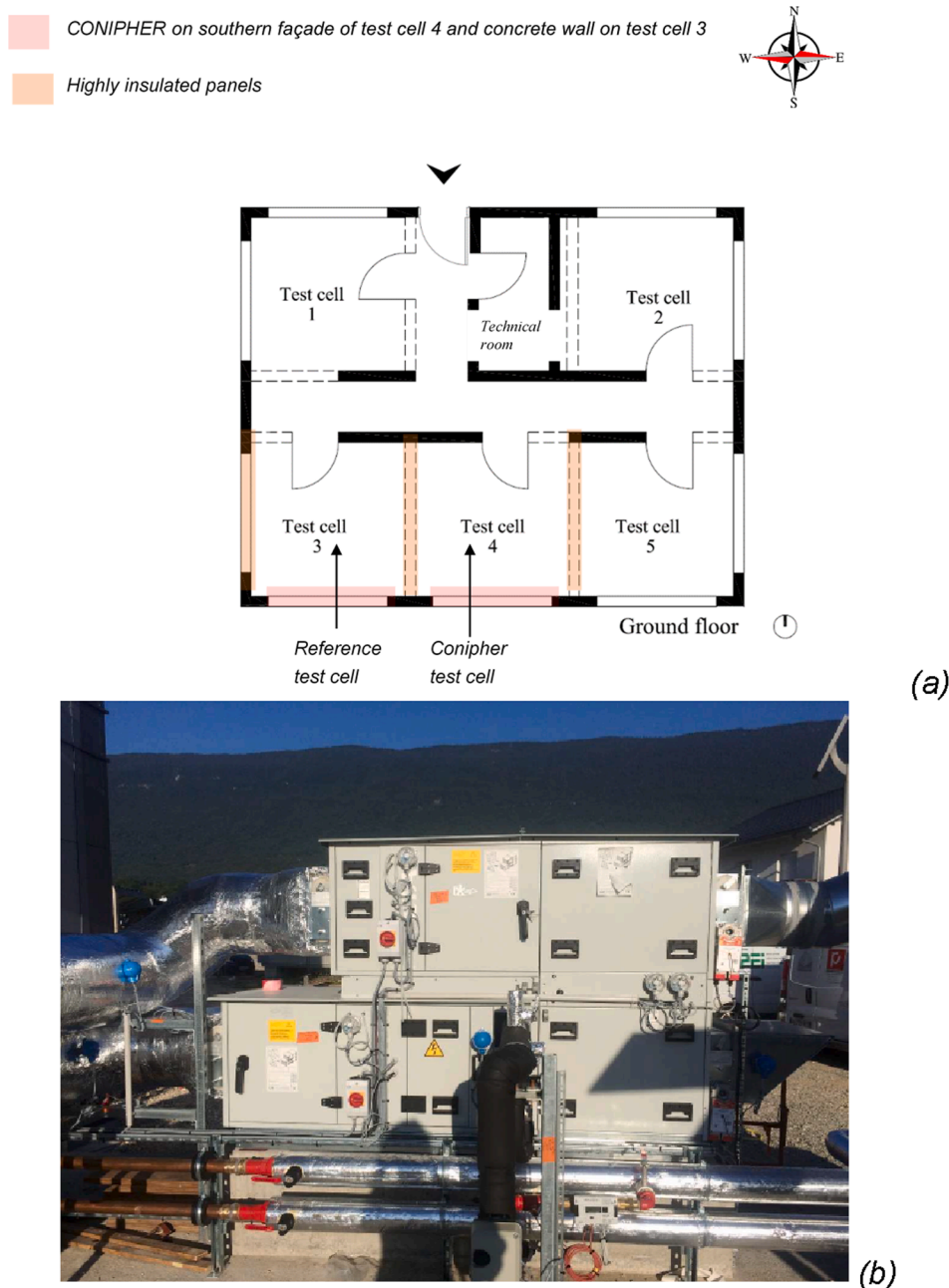


Fig. 5. Location of the test cell 3 and the test cell 4 on a plan of FACT tool ground floor (a) and dual-flow air handling unit (CIAT) (b).

Finally, a bifacial gain BG was evaluated using Eq. (6):

$$BG = (E_{ac} - E_{pvmf}) / E_{pvmf} \tag{6}$$

With  $E_{pvmf}$  the electrical energy production (kWh) of the mono-facial BIPV facade calculated based on the numerical integration of Eq. (5) on a defined period (time step in hour).

#### 4. Analysis of the bifacial photovoltaic PV module thermal behavior

In this section, the thermal behavior of the bifacial photovoltaic facade is analyzed on daily and monthly bases focusing on the PV modules. The PV module 3 and the PV module 5 were mainly studied since they were the most instrumented (see Fig. 6b). The PV module 3 is located below the PV module 5 on the solar facade (see Fig. 6a).

##### 4.1. Analysis of the bifacial PV modules thermal behavior on a daily base

In July 2019, the solar radiation in the vertical plane was up to 554.2  $W/m^2$  with a cumulated total solar energy of 51  $kWh/m^2$ . It is to be noted that due to FACT tool annual maintenance, some measured data were missing from the 8th to the 21st of July (see Fig. 8a). The ambient temperature was comprised between 14.7 °C and 40.7 °C (see and Fig. 8b).

In January 2019, the maximum solar radiation in the vertical plane was of 295  $W/m^2$  with a cumulated total solar energy of 56  $kWh/m^2$  (see Fig. 9a) and the ambient temperature was between -5 °C and 12.1 °C (see Fig. 9b).

Figs. 8b and 9b present daily temperatures profiles of the PV module 3 and the PV module 5 during respectively, a month in warm period (in July 2019) and a month in cold period (in January 2019) and the corresponding outdoor ambient air temperature profiles.

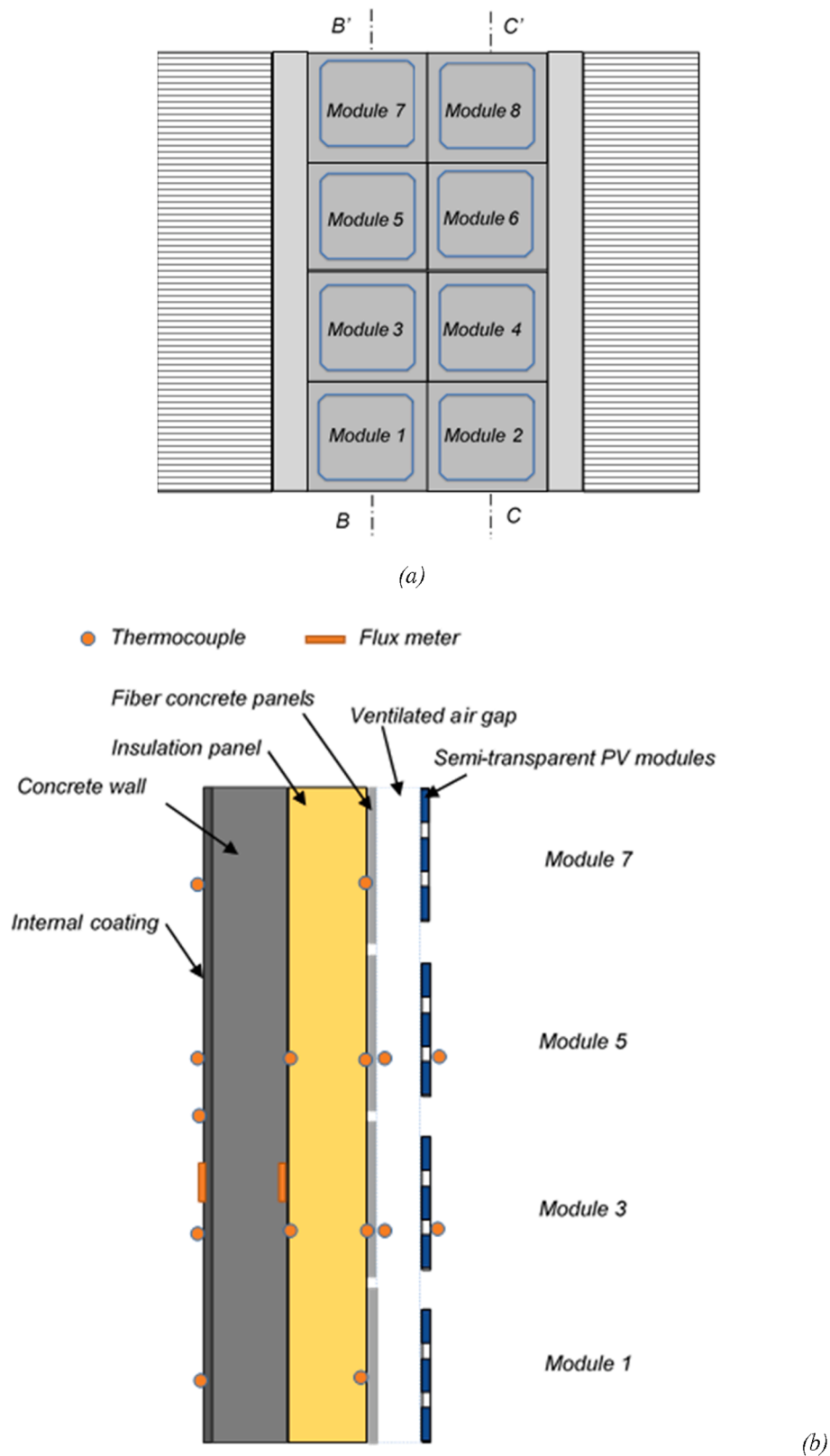


Fig. 6. Schemes of the photovoltaic facade front view on test cell 4 (a) and its vertical sections (b: section B'-B and c: section C'-C) and of the vertical section of the reference facade on test cell 3 (d) (with orange lines for flux meters and orange dots for thermocouples).

Figs. 8b and 9 b show that the PV module 3 temperature was comprised between  $-4.5\text{ }^{\circ}\text{C}$  and  $51.8\text{ }^{\circ}\text{C}$  in January and between  $15.2\text{ }^{\circ}\text{C}$  and  $64.2\text{ }^{\circ}\text{C}$  in July, while the PV module 5 temperature was comprised

between  $-4.3\text{ }^{\circ}\text{C}$  and  $57.9\text{ }^{\circ}\text{C}$  in January and between  $15.5\text{ }^{\circ}\text{C}$  and  $65.1\text{ }^{\circ}\text{C}$  in July. The PV module 5 temperature was higher than the PV module 3 temperature, which could be explained by the predominant



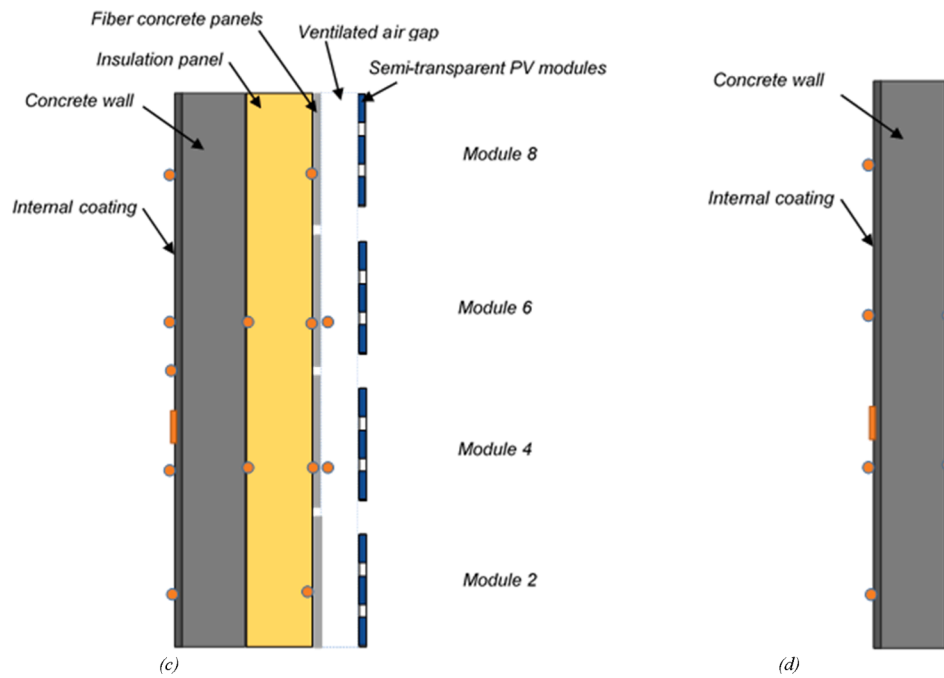


Fig. 6. (continued).

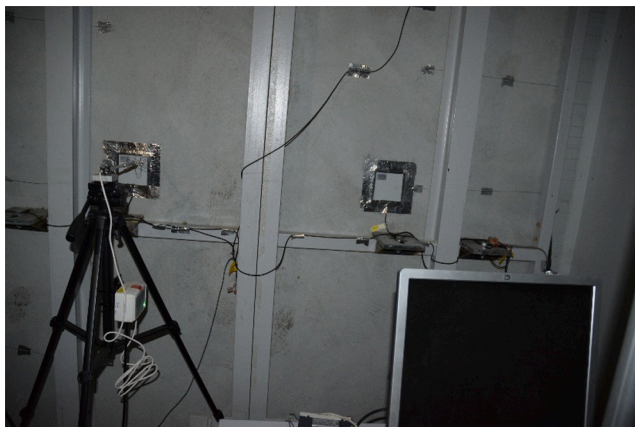


Fig. 7. Photograph of the interior of the test cell 4 with some thermocouples and flux meters (behind PV module 3 (at the right side) and at the level of the interface between PV modules 3 and 4 (at the left side)) on the internal coating and with the anemometer of Delta Ohms.

rising stack effect (natural ventilation due to air pressure drops and wind effects at the inlets and the outlets of the air gap) (Brinkworth et al., 2000) in the discontinuous air gap (Sanjuan et al., 2011b) compared to site albedo impact (solar radiation reflected by site elements (ground, front building, mountains and airport)). In January, the thermal gradient between the PV module 3 and the PV module 5 was comprised between  $-0.2\text{ }^{\circ}\text{C}$  and  $10.4\text{ }^{\circ}\text{C}$  with higher differences during daylight hours. However, in July, this thermal gradient was reduced (between  $-1.3\text{ }^{\circ}\text{C}$  and  $3.7\text{ }^{\circ}\text{C}$ ) due to the most important effect of site albedo increasing PV modules temperature at the bottom of the facade.

Then, the PV module 3 heating compared to outdoor ambient temperature was between  $-3.7\text{ }^{\circ}\text{C}$  and  $28.7\text{ }^{\circ}\text{C}$  in July and between  $-5.3\text{ }^{\circ}\text{C}$  and  $50.3\text{ }^{\circ}\text{C}$  in January, with negative values during night, as expected, due to heat transfer by radiation with the sky. The PV module 5 heating was between  $-3.4\text{ }^{\circ}\text{C}$  and  $29.4\text{ }^{\circ}\text{C}$  in July and between  $-5.2\text{ }^{\circ}\text{C}$  and  $60.4\text{ }^{\circ}\text{C}$  in January (see Figs. 8b and 9b).

Furthermore, the PV modules thermal behavior was analyzed on a

Table 3

Uncertainties of the measurement sensors.

Sensors	Uncertainty and sensitivity
T-type thermocouple of TC SA	Less or equal to 2%;
CS215 perforated PT100 probe of Campbell Scientific	$\pm 0.3\text{ }^{\circ}\text{C}$ at $25\text{ }^{\circ}\text{C}$ ; $\pm 0.4\text{ }^{\circ}\text{C}$ (between $+5$ and $+40\text{ }^{\circ}\text{C}$ ); $\pm 0.9\text{ }^{\circ}\text{C}$ (between $-40$ and $+70\text{ }^{\circ}\text{C}$ );
Anemometer of Delta Ohms	$\pm 0.05\text{ m/s}$ ( $k = 2$ ) for an air velocity of $1\text{ m/s}$ ;
Ultrasonic anemometer Windsonic WS3 of Gill Instruments	$\pm 2\%$ for wind velocity range between $0$ and $60\text{ m/s}$ ; $\pm 3\%$ for wind direction range between $0$ and $359^{\circ}$ ;
Pyranometer CMP11 of Kipp & Zonen	$\pm 1.4\%$ ;
Hukseflux HFP01-L heat flux sensor of Campbell scientific	Within $-15\%$ to $+5\%$ in most common soils for $12\text{ h}$ ;
BCAM thermal camera of Flir Systems	$\pm 2\text{ }^{\circ}\text{C}$ or $\pm 2\%$ of reading (between $-10$ and $+100\text{ }^{\circ}\text{C}$ ) (default auto-adjusted emissivity: $0.96$ );
34972A datalogger of Agilent	$\pm 0.0035\%$ of reading $\pm 0.005\%$ of selected range;
SHARKY 775 energy meter of DHIEL	$\pm 10\%$ on thermal power (positive values for heating periods and negative values for cooling periods).

monthly base.

#### 4.2. Analysis of the bifacial PV modules thermal behavior on a monthly base

Table 4 presents the monthly maximum temperatures of the PV module 3 and the PV module 5 on the testing period.

According to results of Table 4, the PV module 5 reached maximum temperatures of nearly  $69.3\text{ }^{\circ}\text{C}$  in autumn (in October 2019),  $66.9\text{ }^{\circ}\text{C}$  in winter (in March 2019),  $62.2\text{ }^{\circ}\text{C}$  in spring (in June 2019) and  $70.2\text{ }^{\circ}\text{C}$  in summer (in September 2019) and thus was warmer than the PV module 3 (with respectively,  $64.4\text{ }^{\circ}\text{C}$ ,  $61.6\text{ }^{\circ}\text{C}$ ,  $61.2\text{ }^{\circ}\text{C}$  and  $66.4\text{ }^{\circ}\text{C}$ ).

The gradient of temperatures between the two PV modules was comprised between nearly  $0.9\text{ }^{\circ}\text{C}$  and  $7\text{ }^{\circ}\text{C}$  on the testing period, which could also be explained by the stack effect in the discontinuous air gap and by the solar radiation reflected by the ground on the solar facade

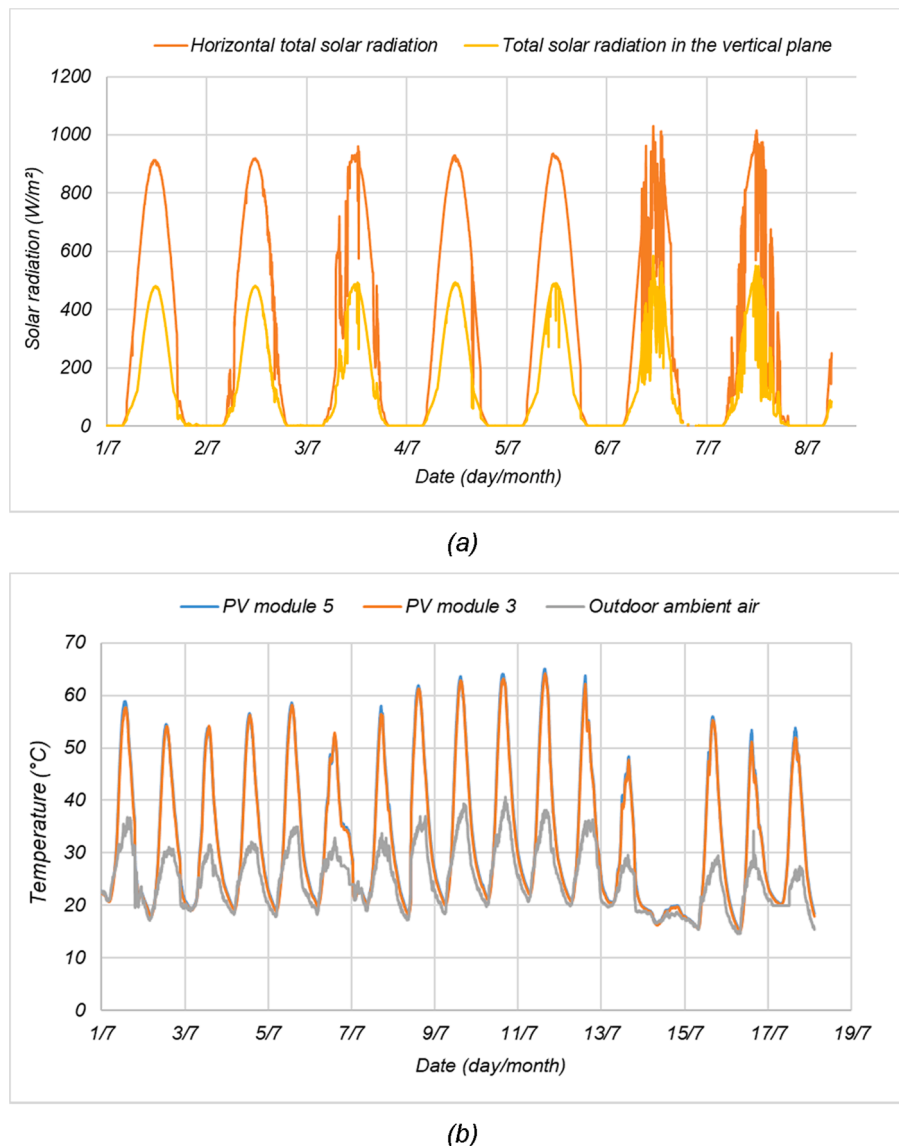


Fig. 8. Horizontal total solar radiation, total solar radiation in the vertical plane (a), temperatures profiles of PV modules 3 and 5 and outdoor ambient air temperature (b) during a month in warm period (in July 2019).

(albedo) (see Table 4). The lower thermal gradients observed in warm period (between 0.9 °C and 3.9 °C from April 2019 to August 2019) could be due to an albedo effect enhanced by the higher sun height and solar radiation intensities (see Table 4 and Fig. 8b).

In mid-season and cold period, the higher gradients of temperatures between the PV module 5 and the PV module 3 (between 3.8 °C and 7 °C from December 2018 to March 2019 and from September 2019 to December 2019) could be due to lower sun height limiting the albedo effect (see Table 4).

Then, Fig. 10 presents the monthly variations and the average values of the PV field mean temperatures (obtained based on the PV module 3 and the PV module 5 measured temperatures) from December 2018 to December 2019 (see Fig. 10). Temperature sensors were stuck on the front glass edge, so, the temperatures of PV cells could be slightly higher than the measured values since the thermal conductivity of glass (of nearly 1 W/m K) is lower than the one of the monocrystalline silicon PV cells (between 100 W/m K and 140 W/m K).

As expected, in cold season, lower PV field monthly average temperatures are observed (from December 2018 to March 2019 and from October 2019 to December 2019) with values comprised between 7.4 °C in January 2019 and 21.3 °C in October 2019. In warm season (from

April 2019 to September 2019), the PV field monthly average temperatures were comprised between 20.4 °C in April 2019 and 32.6 °C in July 2019.

Considering the whole testing period, the PV field mean temperatures varied between −4.4 °C in January 2019 and 68.3 °C in September 2019. In warm season, the PV field mean temperatures were comprised between 0.9 °C in April 2019 and 68.3 °C in September 2019. The higher level of temperatures compared to cold season is due to more important solar radiation intensities and outdoor ambient air temperatures. In cold season, the PV modules mean temperatures were between −4.4 °C in January 2019 and 66.9 °C in October 2019. High temperatures values noted in cold season could be explained by the better sun exposure (lower sun height) for a facade integrated system and by the lower stack effect in the air gap (lower thermal gradient between the top and the bottom of the facade) (see Fig. 10).

Then, since all photovoltaic modules could not be instrumented, a thermal camera was used to analyze the gradient of temperatures along the bifacial facade in a warm day and in a cold day.

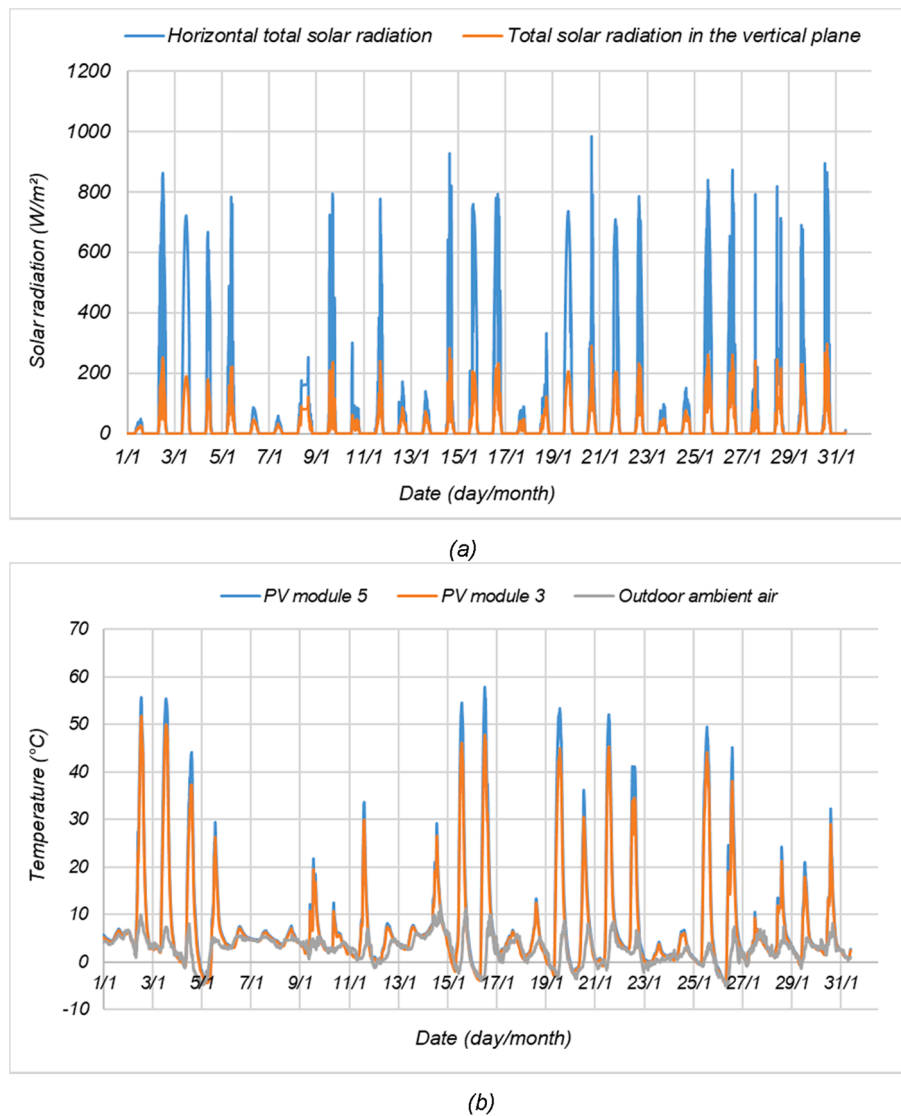


**Fig. 9.** Horizontal total solar radiation, total solar radiation in the vertical plane (a), temperatures profiles of PV modules 3 and 5 and outdoor ambient air temperature (b) during a month in cold period (in January 2019).

**Table 4**  
Monthly maximum temperatures of the PV module 3 (Tpv3) and the PV module 5 (Tpv5) and absolute difference of temperatures (dTpv) taking Tpv5 as reference from December 2018 to December 2019.

Month and year	Tpv3 (°C)	Tpv5 (°C)	dTpv (°C)
December 2018	51.7	58.2	6.5
January 2019	51.8	57.9	6.1
February 2019	60.6	66.8	6.2
March 2019	61.6	66.9	5.2
April 2019	58.1	62.0	3.9
May 2019	52.3	53.4	1.2
June 2019	61.2	62.2	1.1
July 2019	64.2	65.1	0.9
August 2019	66.2	68.6	2.4
September 2019	66.4	70.2	3.8
October 2019	64.4	69.3	4.9
November 2019	50.9	57.9	7.0
December 2019	51.0	57.7	6.7

**5. Analysis of the temperature distribution on the bifacial photovoltaic facade**

The thermal behavior of the bifacial photovoltaic facade is analyzed

on a daily base focusing on the whole system. The temperature distribution on the indoor side and the outdoor side of the PV facade was studied using a thermal camera (see Table 3) in order to estimate the impact of stack effect and of site albedo and to observe the possible existing thermal bridges between the bifacial PV facade basic elements. A day with a low level of solar radiation and a day with a high level of solar radiation were considered.

**5.1. Temperature distribution at low solar radiation level**

Fig. 11 presents the thermal images obtained on a day in April with low level of solar radiation from 1:58 pm to 2:01 pm. The mean solar radiation on the vertical plane was of nearly 58.3 W/m<sup>2</sup> (of nearly 111.1 W/m<sup>2</sup> on the horizontal plane), the mean outdoor ambient air temperature was of 15.1 °C and the mean wind velocity was of nearly 2 m/s on this short period.

At low solar radiation, a reduced gradient of temperatures is noted along the facade (limited temperature range of nearly 5 °C) (see Fig. 11a) with the fasteners at nearly 12.7 °C (see Fig. 11c), the PV module 1 and the PV module 2 at 17.1 °C (see Fig. 11d) and the concrete wall between the PV modules 1, 2, 3 and 4 at nearly 19.3 °C (see Fig. 11b).

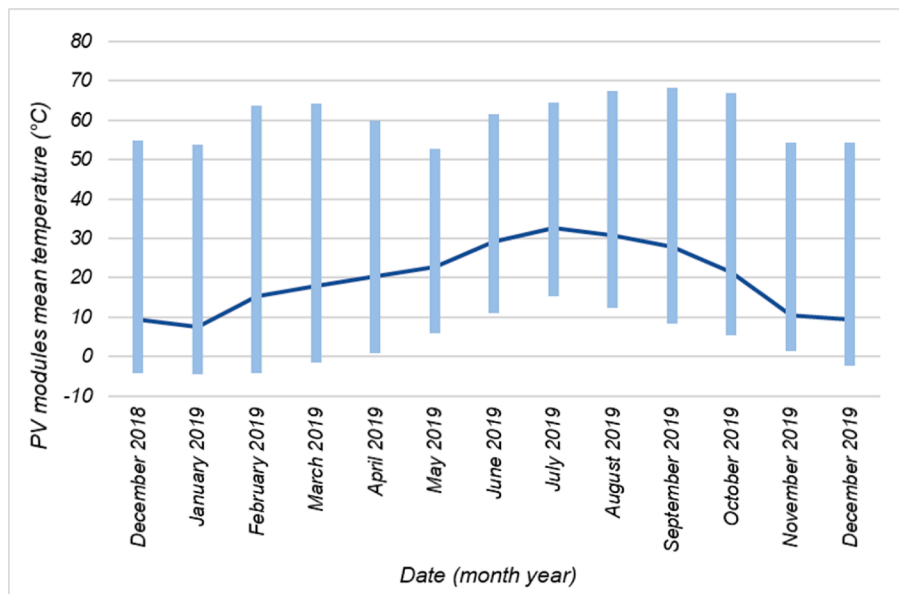


Fig. 10. Monthly variations of the PV field mean temperature based on the PV modules 3 and 5 front glass temperatures and monthly average values (dark blue line) from December 2018 to December 2019.

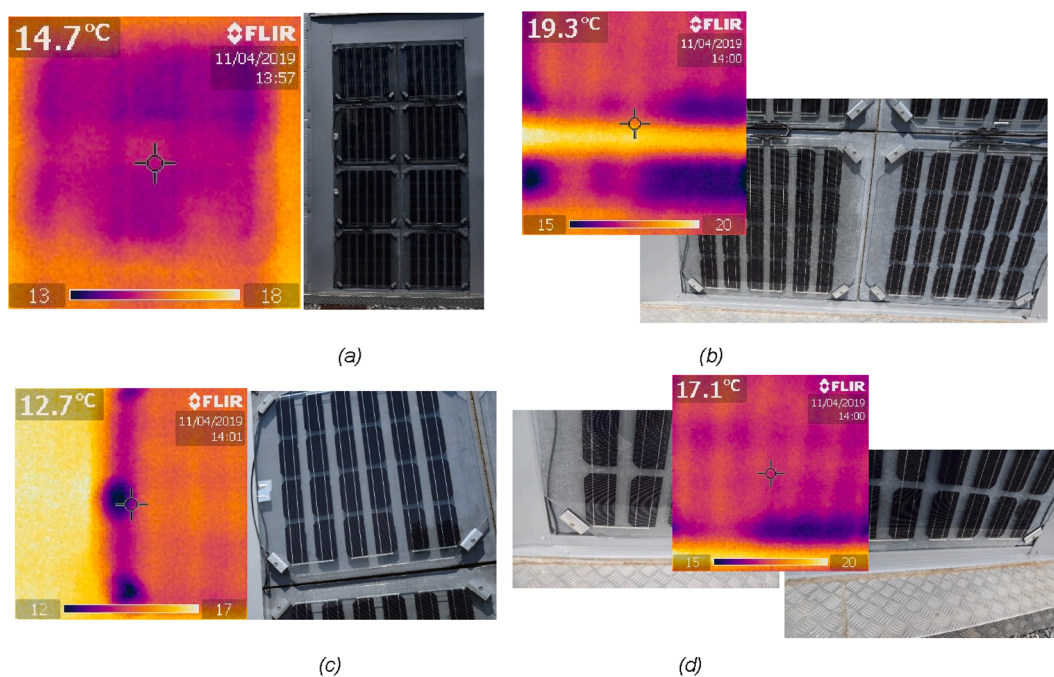


Fig. 11. Thermal images and photographs of the BIPV facade on test cell 4 from 1:58 pm to 2:00 pm on a day in April with low solar radiation: (a) on the PV field; (b) at the interface between PV modules 1, 2, 3 and 4; (c) on fasteners of PV module 3 and (d) on PV module 1 and PV module 2.

The slightly higher temperature observed at the interfaces between the bifacial photovoltaic facade basic elements could be explained by the direct heat storage in the concrete wall, although the sun exposed areas are very thin (see Fig. 11b).

Fig. 12 shows the photographs (see Fig. 12a and c) and the thermal images (see Fig. 12b and d) of the internal coatings of the solar facade on test cell 4 and the reference facade on test cell 3 from 2:12 pm to 2:21 pm on the same day. The mean solar radiation on the vertical plane was of 47 W/m<sup>2</sup> nearly (124 W/m<sup>2</sup> nearly on the horizontal plane), the mean ambient temperature was of 14.8 °C nearly and the mean wind velocity was of nearly 2.3 m/s on this period.

The temperature at the center of the internal coating was of 17.5 °C

in test cell 3 (reference) (see Fig. 12d) and of 22.8 °C in test cell 4 (see Fig. 12b), in these conditions. Thus, the integration of the bifacial photovoltaic facade has led to an increase of the coating temperature of nearly 5.3 °C during the testing period and to a reduction of heat transfers through the wall since its temperature is closer to the setpoint temperature in April 2019.

### 5.2. Temperature distribution at high solar radiation level

A similar analysis was performed on a day in May 2019 with more important solar radiation from 1:34 pm to 1:44 pm. The mean solar radiation on the vertical plane was of 365 W/m<sup>2</sup> nearly (of nearly 661

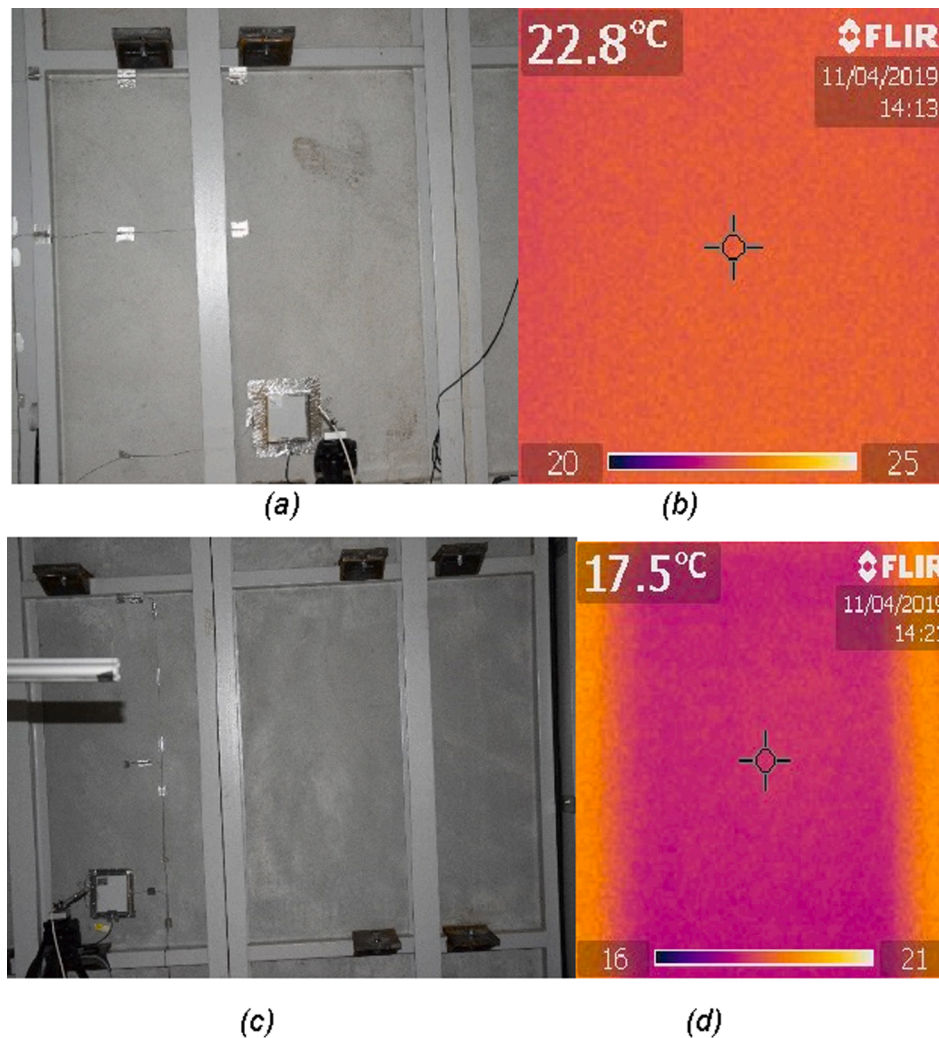


Fig. 12. Photographs and thermal images of the internal coatings of the south-oriented facades of test cell 4 (a and b) and test cell 3 (c and d) from 2:12 pm to 2:21 pm on a day in April with low solar radiation.

$W/m^2$  on the horizontal plane), the mean ambient temperature was of nearly  $21.1\text{ }^\circ\text{C}$  and the mean wind velocity was of nearly  $2.8\text{ m/s}$ .

Fig. 13 presents the thermal images and the photographs of the BIPV facade on test cell 4, during this short period (see Fig. 13).

A more important thermal gradient is observed, as expected, along the BIPV facade with temperatures of fasteners of nearly  $34.1\text{ }^\circ\text{C}$  (see Fig. 13c), of an edge of PV module 4 of nearly  $40.9\text{ }^\circ\text{C}$  (see Figs. 6a and 13a), of the concrete wall at the interface of PV modules 1, 2, 3 and 4 comprised between  $46.6\text{ }^\circ\text{C}$  and  $54.6\text{ }^\circ\text{C}$  (see Fig. 13b) and of the concrete wall at the interface of PV modules 3, 4, 5 and 6 of nearly  $50.7\text{ }^\circ\text{C}$  (see Fig. 13d).

Except for the PV modules located at the bottom of the wall, the PV facade temperature increases slowly from bottom to top due to both the stack effect and the site albedo effect, which are more significant at high solar radiation than at low solar radiation, as expected. Since the air gap is discontinuous and comprises different entries, the gradient of temperatures is not uniform from bottom to top like in a conventional PV ventilated facade. Indeed, the outdoor air entering the air gap is cooler than the PV modules and the fiber concrete panel and thus, reduces their temperatures (Sanjuan et al., 2011b). According to Sanjuan et al. (2011a), in the case of the studied open joint ventilated solar facade, this outdoor air tends to enter in the air gap at the bottom and the top of the first row of PV modules (see PV modules 1 and 2 in Fig. 6a) and to exit at the bottom and top of the upper row of PV modules (see PV modules 7 and 8 in Fig. 6a) (see Fig. 2c).

Moreover, Fig. 13 highlights that the existing site albedo seems to have, here, a preponderant influence compared to the stack effect at high solar radiation conditions and in warm period due to higher sun height. The albedo effect is, as expected, more important close to the ground (which is composed of white and light grey gravels with a high reflection coefficient) and decreases gradually from the bottom to the top of the facade (Raybaud et al., 2019).

Since the PV modules are connected in series on the micro-inverter, this important thermal gradient along the facade could reduce the system electrical performance compared to a more uniform facade temperature distribution.

A darker ground could limit this effect and in the case of bifacial modules installation, a thicker air gap could increase the incident solar radiation rate reflected by the fiber concrete panel and reaching the PV modules backside. Therefore, a suitable choice of the surrounding ground type close to the PV facade could improve its thermal behavior and then its electrical production. Moreover, the increase of the air gap thickness (from 2 cm to 5 cm, for example) could improve the cooling of PV modules at their rear side (Lau et al., 2018) and thus their electrical production.

These approaches could be included at design phase for the architectural development of fully integrated BIPV solutions (Farkas et al., 2013).

Finally, Fig. 14 shows the thermal images and the photographs of the internal coatings of the solar facade on test cell 4 and of the reference

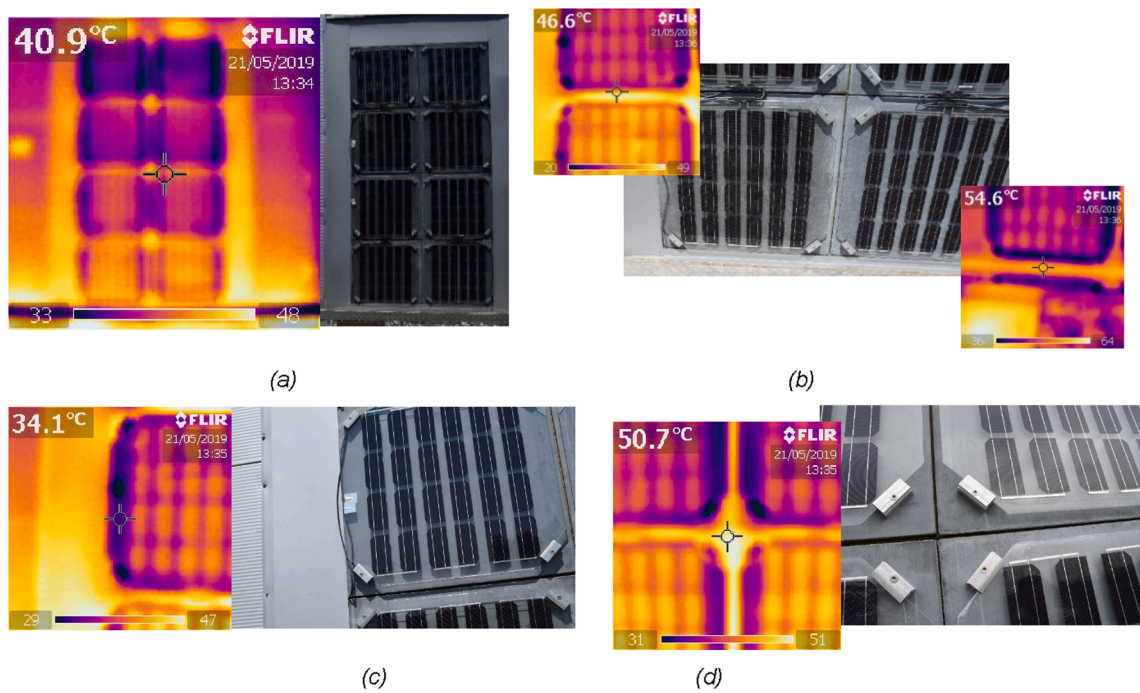


Fig. 13. Thermal images and photographs of the BIPV facade on test cell 4 from 1:34 pm to 1:44 pm on a day in May with high solar radiation: (a) on the PV field; (b) at the interface between PV modules 1, 2, 3 and 4; (c) on fasteners of PV module 3 and (d) at the interface between PV modules 3, 4, 5 and 6.

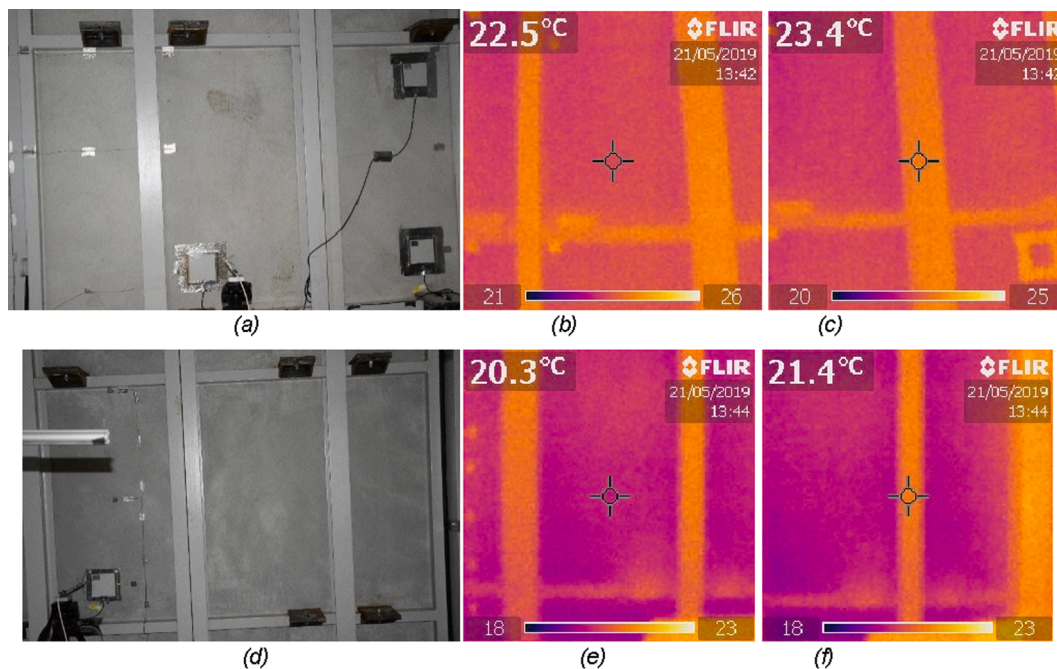


Fig. 14. Photographs and thermal images of the internal coatings of the south-oriented facades of test cell 4 (a, b and c) and of test cell 3 (d, e and f) obtained with a thermal camera from 1:34 to 1:44 pm on a day in May with high solar radiation.

facade on test cell 3 at higher solar radiation between 1:42 pm and 1:44 pm on the same day (see Fig. 14). The mean solar radiation on the vertical plane was of  $500 \text{ W/m}^2$  nearly (of  $943 \text{ W/m}^2$  nearly on the horizontal plane), the mean outdoor ambient air temperature was of  $22.2 \text{ }^\circ\text{C}$  and the mean wind velocity of nearly  $1.24 \text{ m/s}$ , on this period.

As expected, lower surface temperatures are noted in test cell 3 (of  $20.3 \text{ }^\circ\text{C}$  for the metal structure and of  $21.4 \text{ }^\circ\text{C}$  for the internal coating) (see Fig. 14e and f) compared to test cell 4 (of  $23.4 \text{ }^\circ\text{C}$  for the metal structure and of  $22.5 \text{ }^\circ\text{C}$  for the indoor coating) (see Fig. 14b and c).

Results show that at higher solar radiation, there is a lower increase of coating temperature (of  $2.2 \text{ }^\circ\text{C}$  nearly) after integration of the bifacial PV facade elements, on the selected testing period. This seems to be due to the more optimal weather conditions (solar radiation and outdoor ambient air temperature) permitting an improved heat storage in the reference concrete wall on test cell 3 and to a better heat extraction (stack effect) in the solar facade air gap on test cell 4 leading to a better cooling of the fiber concrete wall and of the bifacial PV modules.

At low and high solar radiation levels, the uniformity of the internal

coating temperature distribution (see Figs. 12 and 14) compared to the important thermal gradient on the outside (see Figs. 10 and 12) of the bifacial BIPV facade highlights also that the developed system configuration permits satisfactorily to limit the impact of the possible thermal bridges at the interfaces of the PV basic elements. It is to be noted that results obtained with thermal camera are consistent with the values of Figs. 8b, 9b and Table 4.

## 6. Analysis of the bifacial photovoltaic modules electrical performance

### 6.1. Analysis of the bifacial photovoltaic facade electrical performance

The electrical production of the PV field of 456 Wp was measured mainly in order to estimate the impact of building integration on bifacial PV modules performance. Table 5 summarizes the system monthly electrical performance after micro-inverter (AC) (energy production, final yield, performance ratio and efficiency), the outdoor ambient air temperature and the cumulated incident solar energy from December 2018 to December 2019 and their annual cumulated or mean values.

Fig. 15 presents the monthly electrical energy production and the performance ratio after micro-inverter (AC) of the system studied on the selected period.

Table 5 and Fig. 15 indicate, as expected, a decrease of performance in warm season (from April to September 2019) due to higher levels of the PV modules temperature and more optimal incident angles of solar radiation.

The monthly solar energy produced was comprised between 31 kWh/m<sup>2</sup> and 111 kWh/m<sup>2</sup> nearly during the two cold seasons and between 51 kWh/m<sup>2</sup> and 111 kWh/m<sup>2</sup> nearly in warm season. The cumulated solar energy on the selected period was of 1009 kWh/m<sup>2</sup> nearly. The lower results obtained in July 2019 and November 2019 are due to monitoring issues and to the site maintenance period.

In cold season, from December 2018 to March 2019 and from October 2019 to December 2019, the monthly electrical energy production was comprised between 2 kWh/m<sup>2</sup> and 7.4 kWh/m<sup>2</sup> nearly corresponding to electrical efficiencies between 6.3% and 7% and to performance ratio between 0.736 and 0.806. The monthly final yield was between 23.5 kWh/kWp and 88.9 kWh/kWp and maximum values were obtained in February 2019.

In warm season, from April 2019 to September 2019, the monthly

electrical energy production was comprised between 2.8 kWh/m<sup>2</sup> and 6.9 kWh/m<sup>2</sup> corresponding to electrical efficiencies between 5.6% and 6.4% and to performance ratio between 0.647 and 0.737. The monthly final yield was between 32.8 kWh/kWp and 80.1 kWh/kWp with maximum values in September 2019 (see Table 5 and Fig. 15). The variations of performance ratio values on the testing period highlight optimal electrical performance in cold season, as expected.

The cumulated electrical energy produced was of 63.8 kWh/m<sup>2</sup> considering the whole period and of 60.9 kWh/m<sup>2</sup> on the year (from December 2018 to November 2019) with 31.5 kWh/m<sup>2</sup> in warm season (from April to September 2019) and 29.4 kWh/m<sup>2</sup> in cold periods (from December 2018 to March 2019 and from October to November 2019). So, although the less optimal operating conditions in warm season for a façade integrated system, the bifacial photovoltaic field permits globally close cumulated electrical energy productions in cold and warm seasons. This could be explained by the rear side additional production of bifacial PV modules, which seems to increase in warm season thanks to the higher impact of site albedo (see Fig. 13a). The lower cumulated energy production in cold season seems to be due to monitoring issue.

The PV system mean annual efficiency was of 6.3% and the total annual final yield was of 706.1 kWh/kWp (of 739.9 kWh/kWp on the whole period). The mean annual value of performance ratio of 0.73 indicates that the level of ventilation of PV modules at the rear side is average due to the low air gap thickness (of 2 cm). Nevertheless, this value indicates also that the facade integrated bifacial PV field provided nearly 73% of its expected electrical energy production in STC conditions and in a non-integrated configuration, and up to 80.6% in February, which is satisfactory.

### 6.2. Impact of bifaciality on the photovoltaic system electrical performance

Then, the monthly impact of bifaciality on the photovoltaic system electrical performance was analyzed on the testing period based on a comparison with a photovoltaic facade comprising monofacial PV modules with electrical characteristics in STC similar to the ones of the bifacial PV modules front side. Eqs. (4) and (5) were used to calculate the electrical energy production of the monofacial facade since this installation could not be tested on site and the monthly, annual, and period bifacial gains were obtained with Eq. (6) (see Eqs. (4)–(6) and Table 6).

**Table 5**

Monthly, period and annual (cumulated or mean) electrical performance after micro-inverter (AC) of the bifacial BIPV facade (electrical energy production, final yield, performance ratio and electrical efficiency), outdoor ambient air temperature (minimum, maximum and mean values) and incident total solar energy from December 2018 to December 2019.

Month	Ambient air temperature ([min; max]; mean) (°C)	Cumulated total solar energy in the vertical plane (kWh/m <sup>2</sup> )	Cumulated electrical energy production (AC) (kWh/m <sup>2</sup> )	Final yield (kWh/kWp)	Performance ratio (–)	Electrical efficiency (%)
December 2018	[–4.2;16.4]; 5.7	44	2.9	33.4	0.8	6.5
January 2019	[–5; 12.1]; 2.8	56	3.8	44.4	0.792	6.8
February 2019	[–4.5; 21.2]; 4.8	110	7.7	88.9	0.806	7.0
March 2019	[–1.7; 24]; 9.1	111	7.4	85.8	0.776	6.7
April 2019	[0.4; 27]; 12	98	6.2	71.9	0.737	6.4
May 2019	[0.6; 28.1]; 14.2	79	4.8	55.6	0.707	6.1
June 2019	[9.2; 38.2]; 21.6	80	4.5	52.1	0.655	5.6
July 2019	[14.7; 40.7]; 11.6	51	2.8	32.8	0.647	5.6
August 2019	[11.2; 37.1]; 22.1	108	6.2	72.4	0.673	5.8
September 2019	[7.5; 32.1]; 18.3	111	6.9	80.1	0.723	6.2
October 2019	[5; 26.1]; 14.2	86	5.6	65.2	0.756	6.5
November 2019	[0; 59]; 29.5	31	2.0	23.5	0.756	6.5
December 2019	[2.0;17.5]; 6.1	46	2.9	33.8	0.736	6.3
Total or mean values (from December 2018 to December 2019)	–	1009 (total)	63.8 (total)	739.9 (total)	0.730 (mean)	6.3 (mean)
Annual total or mean values (from December 2018 to November 2019)	–	964 (total)	60.9 (total)	706.1 (total)	0.732 (mean)	6.3 (mean)

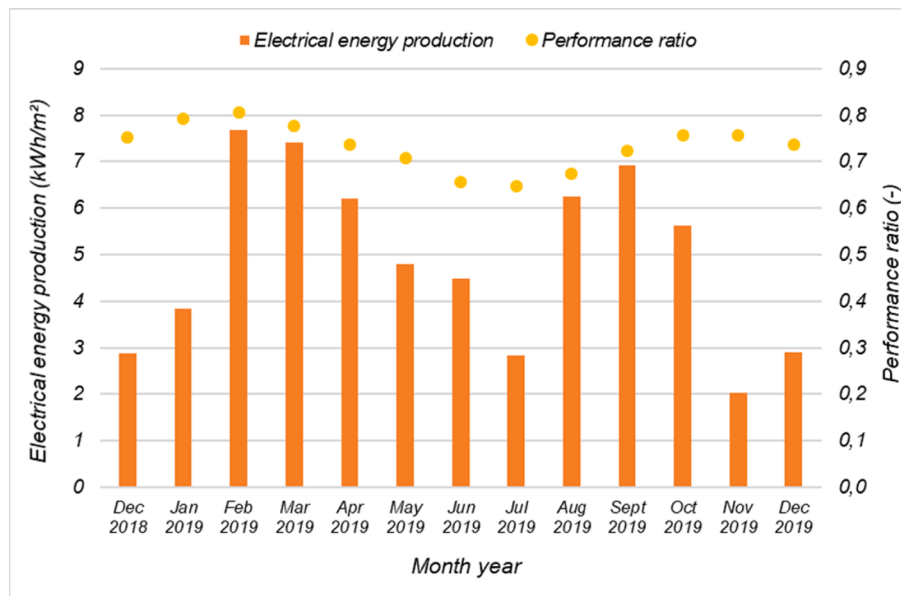


Fig. 15. Monthly electrical energy production and performance ratio after micro-inverter (AC) of the bifacial BIPV facade from December 2018 to December 2019.

Table 6

Monthly, period and annual cumulated electrical performance after micro-inverter (AC) (kWh) of the bifacial BIPV façade and of the monofacial BIPV façade and bifacial gains from December 2018 to December 2019.

Month	Cumulated electrical energy production of the bifacial BIPV facade (kWh)	Cumulated electrical energy production of the monofacial BIPV facade (kWh) (calculated)	Bifacial gain (%)
December 2018	15.9	12.5	26.38
January 2019	20.3	15.8	28.09
February 2019	40.6	29.5	37.49
March 2019	39.1	29.9	30.77
April 2019	32.8	26.6	23.19
May 2019	25.4	22.2	14.08
June 2019	19.8	19.0	4.51
July 2019	6.8	6.1	11.03
August 2019	33.0	28.2	17.28
September 2019	33.0	29.1	13.48
October 2019	29.7	23.0	29.00
November 2019	10.7	8.7	23.35
December 2019	15.4	12.8	20.46
Period (cumulated)	322.3	263.4	22.38
Year (cumulated)	307.0	250.62	22.48

Table 6 shows that the monofacial PV system has a lower electrical energy production than the bifacial PV system, as expected.

The bifacial gains were comprised between 4.51% (in June 2019) and 37.49% (in February 2019).

The mean bifacial gains on the selected period and on the year were of respectively, nearly 22.38% and 22.48%, which are coherent with the one obtained numerically by Soria et al. (2015) for a facade integration (of nearly 25%). These satisfactory results validate the relevance of the choice of the smooth fiber concrete layer as reflective surface. Nevertheless, a comparison with data measured on a monofacial PV facade should be performed in order to confirm the observations since the calculated results depend on the performance loss coefficient  $C_p$  considered.

Then, the impact of the studied system on the building energy consumption for heating and cooling was estimated experimentally.

## 7. Impact on the building energy performance

### 7.1. Analysis of the building energy consumption

The impact of the solar prototype on the test cell energy consumption

was also evaluated from December 2018 to December 2019. Table 7 summarizes the measured monthly and period cumulated results of energy consumption for heating and cooling and of the total energy consumption needed to maintain the setpoint temperature in the two test cells and the energy savings thanks to the integration of the bifacial BIPV facade calculated taking the test cell 3 results as reference. The total energy consumption is the sum of energy consumptions (in absolute values) for heating and cooling on a defined period.

Results of Table 7 indicates that the integration of the developed bifacial BIPV facade permitted a reduction of the total energy consumption up to 92% (reached in March 2019). In warm season, the total energy consumption was comprised between 60 kWh (in March 2019) and 282 kWh (in July 2019) in the reference test cell (test cell 3) and between 10 kWh (in March 2019) and 145 kWh (in June 2019) in the test cell 4. The reduction of energy consumption in the test cell 4 was between -83% (in April 2019) and -31% (in May 2019) compared to the test cell 3 results.

In cold seasons, the total energy consumption was between 39 kWh (in September 2019) and 409 kWh (in January 2019) in the reference test cell and between 13 kWh (in November 2019) and 48 kWh (in January 2019) in the test cell 4. The decrease of energy consumption in



**Table 7**

Measured cumulated monthly and period energy consumptions for heating and cooling and total energy consumption needed to maintain the setpoint temperature in the reference test cell 3 (non-insulated concrete wall) and in the test cell 4 with the bifacial BIPV facade (in kWh) and calculated energy savings (relative difference of total energy consumptions in %) from December 2018 to December 2019.

	Prototype energy consumption for Heating (kWh)	Reference energy consumption for Heating (kWh)	Prototype energy consumption for Cooling (kWh)	Reference energy consumption for Cooling (kWh)	Prototype total energy consumption (kWh)	Reference total energy consumption (kWh)	Relative difference of total energy consumptions (%)
December 2018	25	174	9	8	34	182	–81
January 2019	45	409	3	0	48	409	–88
February 2019	27	269	2	0	29	269	–89
March 2019	12	160	2	1	13	160	–92
April 2019	9	59	1	1	10	60	–83
May 2019	6	42	41	26	47	68	–31
June 2019	0	1	145	226	145	227	–36
July 2019	4	3	133	279	137	282	–51
August 2019	0	1	120	256	120	257	–53
September 2019	1	2	83	142	84	143	–41
October 2019	1	3	41	36	42	39	8
November 2019	9	131	3	2	13	133	–90
December 2019	12	126	2	1	14	127	–89
Total values	158	1387	632	1020	636	1963	–68

the test cell 4 was between –92% (in March 2019) and 8% (in October 2019) compared to the test cell 3.

The positive relative difference of total energy consumption noted in October 2019 (of 8%) could be due to the test cell 4 internal door openings (see Fig. 5 a) leading to an increase of energy consumption for cooling.

Then, results show that the BIPV system developed has a higher impact on the test cell total energy consumption in cold season (energy savings between 81 and 92%) and especially on the energy consumption for heating compared to the reference test cell.

Fig. 16 provides the cumulated total energy consumption and energy consumptions for heating and cooling in the two test cells and the relative differences of energy consumption in each case from December 2018 to December 2019.

The cumulated total energy consumption on the whole period was of 636 kWh in test cell 4 and of 1963 kWh in the reference test cell corresponding to a reduction of 68% (see Table 6 and Fig. 16). More precisely, the cumulated energy consumption for heating was of 158 kWh in test cell 4 and of 1387 kWh in the test cell 3, corresponding to a reduction of nearly 89% after the BIPV facade integration. The cumulated energy consumption for cooling was of 632 kWh in test cell 4 and of 1020 kWh in the test cell 3, corresponding to a decrease of nearly 38% (see Fig. 16). The values obtained confirmed that the solar solution designed permits to get closer to the targeted reduction of energy consumption for heating of 60%. These high energy savings values after the BIPV facade integration could be limited in case of heat losses through the other test cell walls.

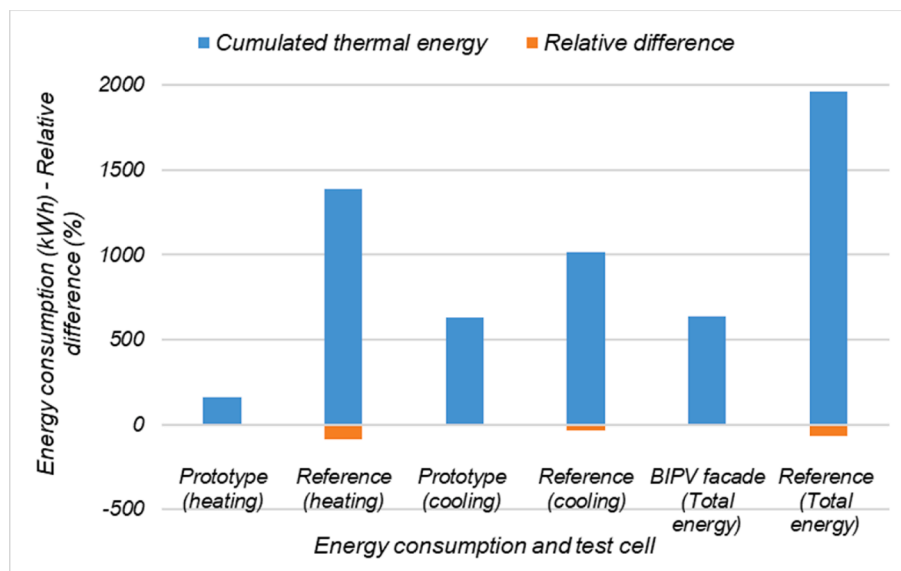


**Fig. 16.** Cumulated values of the total energy consumption and energy consumptions for heating and cooling needed to maintain the setpoint temperature in the test cell 3 (reference) and in the test cell 4 (with the BIPV facade) (in kWh) and relative differences of energy consumption (in %) from December 2018 to December 2019.

## 7.2. Analysis of the impact of the bifacial PV modules on the indoor air temperature on a daily base

The impact of the integration of the bifacial PV modules on air temperature in the test cell was also analyzed on a daily base during a month in cold season and a month in warm season in order to explain the huge reduction of building energy consumption.

Fig. 17 presents the two test cells mean air temperature profiles in July 2019 (warm month) (see Fig. 17a) and in January 2019 (cold season) (see Fig. 17b).

In July 2019, Fig. 17 a shows that most of the time, the air temperature in the test cell 3 (reference) is slightly lower than the air temperature in the test cell 4. The difference of air temperatures taking the test cell 3 as reference is comprised between  $-0.41$  °C and  $1.6$  °C with a mean value of  $0.54$  °C (see Fig. 17a).

In January 2019, similar observations can be made (see Fig. 17b). The difference of air temperatures is between  $-0.63$  °C and  $1.4$  °C with a mean value of  $0.45$  °C (see Fig. 16b).

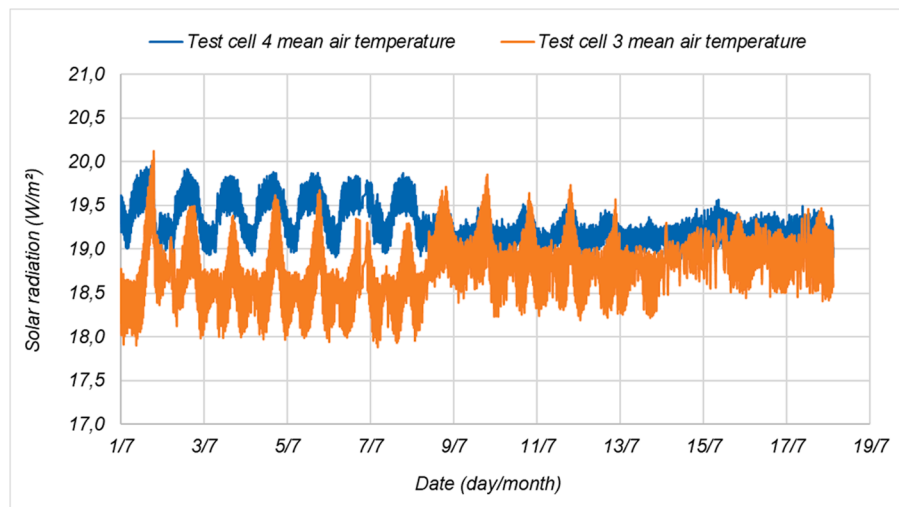
These differences of air temperatures show that the integration of the BIPV system leads heat rise in the test cell 4, reducing heat losses through the initial non-insulated concrete facade (as expected for the test cell 3). Thus, the difference of total energy consumption between the two test cells (see Table 7 and Fig. 16) could be explained by the lower

heat exchanges between the test cell 4 air (convective and radiant) temperature and its BIPV facade compared to heat exchanges between the test cell 3 air temperature and its reference non-insulated concrete facade. Indeed, in the test cell 4, heat exchanges through the facade are mainly influenced by the insulation layer, by the albedo effect, by the fiber concrete panels cooling thanks to stack effect especially in warm season (reducing energy consumption for cooling) and by a greenhouse effect in cold period in the insulated air gap (reducing energy consumption for heating). In the test cell 3, the heat stored in the facade is partially transferred to indoor environment by conduction, convection and radiation.

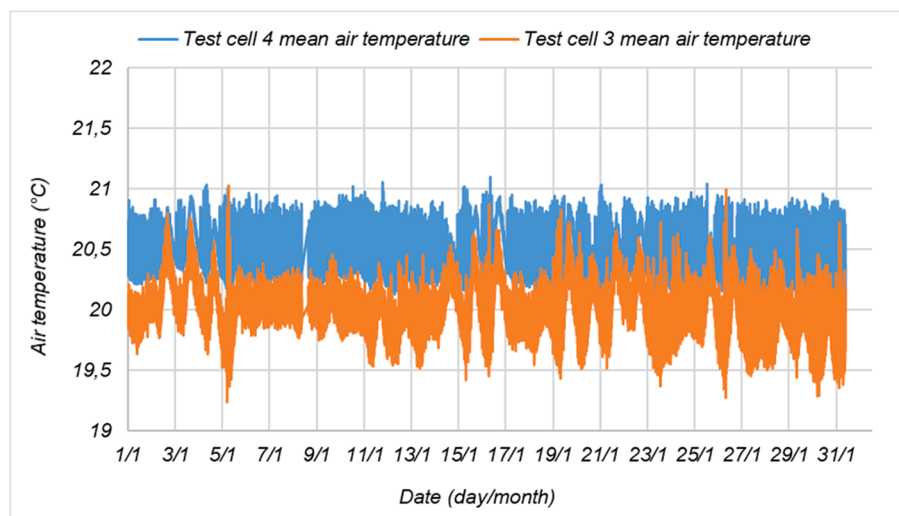
## 8. Conclusion

The innovative bifacial photovoltaic facade element was described. Then, the nearly one year outdoor tests performed on the south-oriented facades of two full-scale test cells at Le Bourget du Lac integrating eight photovoltaic prototypes and a reference non-insulated concrete wall were presented focusing on the monitoring system description and on the analysis of thermal, electrical, energy consumption and weather data on daily, monthly and annual bases.

Based on two instrumented photovoltaic modules, thermal results mainly highlighted daily mean temperatures between  $-4.4$  °C in



(a)



(b)

Fig. 17. Indoor air temperatures profiles of the test cells 3 and 4 in July 2019 (a) and in January 2019 (b).

January 2019 and 68.3 °C in September 2019 and an important monthly thermal gradient up to 7 °C nearly, especially due to the combined impacts of stack effect and site albedo.

Moreover, the photovoltaic field produced a cumulated electrical energy of 63.8 kWh/m<sup>2</sup> corresponding to a performance ratio of 0.73 and a mean annual efficiency of 6.3% from December 2018 to December 2019, which is satisfactory for a façade integrated system. Close cumulated electrical performance in cold period (of 29.4 kWh/m<sup>2</sup>) and in warm period (of 31.5 kWh/m<sup>2</sup>) were observed and could be explained by the rear side additional production of the bifacial PV modules.

Then, the comparison of temperatures distribution on the internal coatings and the outside of the two test cells facades using thermal images showed that the bifacial photovoltaic facade permits a relevant reduction of heat transfers through the concrete wall at low and high solar radiation levels.

Finally, the comparison of total energy consumption (for heating and cooling) of the two tests cells highlighted that the photovoltaic prototype integration permitted an important energy saving up to 92%, especially in cold season. The cumulated total energy consumption was of 636 kWh in the test cell with the solar facade and of 1963 kWh in the reference test cell corresponding to a reduction of 68% on the whole period. The comparative analysis of indoor air temperatures highlighted that the facade integration of the bifacial photovoltaic system seems to permit a management of heat transfers through the initial test cell non-insulated concrete wall. This leads to a reduction of energy consumption for heating and cooling mainly through the wall insulation, the albedo effect, the fiber concrete panels cooling by stack effect in warm season and a greenhouse effect especially in cold period in the insulated air gap. Nevertheless, these important energy savings could be reduced by heat losses through the other test cell walls.

Results obtained in this work contribute to validate the relevance of the integration of bifacial photovoltaic modules into building envelope and thus, to encourage their use in the framework of solar projects, although the less optimal operating conditions for the rear side electrical energy production.

As further studies, the tested configuration will be integrated into an office building in order to demonstrate its performance in real conditions during nearly one year.

## Declaration of Competing Interest

The authors declare that they have no known competing financial interests or personal relationships that could have appeared to influence the work reported in this paper.

## Acknowledgements

This work has been realized in association with INES.2S and is supported by the European Commission and by the LIFE program under project reference LIFE14 CCM/FR/000954.

## References

- ADEME, 2021. La réglementation thermique. Online: <http://www.rt-batiment.fr/IMG/pdf/fiche-travaux-renovation-logement-reglementation-thermique.pdf>.
- Agathokleous, R.A., Kalogirou, S.A., 2016. Double skin facades (DSF) and building integrated photovoltaics (BIPV): A review of configurations and heat transfer characteristics. *Renew. Energy* 89, 743–756.
- Assoa, Y.B., Sauzedde, F., Boillot, B., Boddaert, S., 2017. Development of a building integrated solar photovoltaic/thermal hybrid drying system. *Energy* 128, 755–767.
- Attoye, D.E., Aoul, K.A.T., Hassan, A., 2017. A review on building integrated photovoltaic façade customization potentials. *Sustainability* 9. <https://doi.org/10.3390/su9122287>.
- Brinkworth, B.J., Marshall, R.H., Ibrahim, Z., 2000. A validated model of naturally ventilated PV cladding. *Sol. Energy* 69, 67–81.
- CEA, 2018. Method for manufacturing a photovoltaic element. EP3276673 A1 patent.
- Chen, M., Zhang, W., Xie, L., He, B., Wang, W., Li, J., Li, Z., 2021. Improvement of the electricity performance of bifacial PV module applied on the building envelope. *Energy Build.* 238.
- Chow, T.T., 2003. Performance analysis of photovoltaic-thermal collector by explicit dynamic model. *Sol. Energy* 75, 143–152.
- Cubukcu, M., Gumus, H., 2020. Performance analysis of a grid-connected photovoltaic plant in eastern Turkey. *Sustainable Energy Technol. Assess.* 39 <https://doi.org/10.1016/j.seta.2020.100724>.
- EPD, 2021. The international Environmental Product Declaration system. Online: <https://www.environdec.com/library/epd1848>.
- European Commission, 2020. Online: <https://ec.europa.eu/energy/en/topics/energy-efficiency/energy-performance-of-buildings/energy-performance-buildings-directive#energy-performance-of-buildings-standards>.
- Farkas, K., Frontini, F., Lundgren, M., Maturi, L., Munari Probst, M.C., et al., 2013. Designing photovoltaic systems for architectural integration: Criteria and guidelines for product and system developers. Report T.41.A.3/2: IEA SHC Task 41 Solar Energy and Architecture. Online: <https://task41.iea-shc.org/Data/Sites/1/publications/task41A3-2-Designing-Photovoltaic-Systems-for-Architectural-Integration.pdf>.
- Freitas, S., Brito, M.C., 2019. Solar facades for future cities. *Renew. Energy Focus* 31, 73–79.
- Gu, W., Ma, T., Ahmed, S., Zhang, Y., Peng, J., 2020. A comprehensive review and outlook of bifacial photovoltaic (bPV) technology. *Energy Convers. Manage.* 223 <https://doi.org/10.1016/j.enconman.2020.113283>.
- Han, J., Lu, L., Yang, H., Cheng, Y., 2019. Thermal regulation of PV façade integrated with thin-film solar cells through a naturally ventilated open air channel. *Energy Proc.* 158, 1208–1214.
- Jensen, J.R., 2007. Remote Sensing of the Environment. An Earth Resource Perspective. Pearson Prentice Hall, ISBN-13: 9780134897332, USA.
- Kaldellis, J.K., Kapsali, M., Kavadias, K.A., 2014. Temperature and wind speed impact on the efficiency of PV installations. Experience obtained from outdoor measurements in Greece. *Renew. Energy* 66, 612–624.
- Khalid, A.M., Mitra, I., Warmuth, W., Schacht, V., 2016. Performance ratio—Crucial parameter for grid connected PV plants. *Renew. Sustain. Energy Rev.* 65, 1139–1158.
- Kim, C., Jeong, M.S., Ko, J., Ko, M.G., Kang, M.G., Song, H.-J., 2021. Inhomogeneous rear reflector induced hot-spot risk and power loss in building-integrated bifacial c-Si photovoltaic modules. *Renew. Energy* 163, 825–835.
- Ko, M.G., Lee, G., Kim, C., Lee, Y., Ko, J., Song, H.-J., 2021. Dielectric/metal/dielectric selective reflector for improved energy efficiency of building integrated bifacial c-Si photovoltaic modules. *Curr. Appl. Phys.* 21, 101–106.
- Lau, S.-K., Zhao, Y., Shabunko, V., Chao, Y., Lau, S.-S.-Y., Tablada, A., Reindl, T., 2018. Optimization and evaluation of naturally ventilated BIPV Façade design. *Energy Proc.* 150, 87–93.
- Li, M., Ma, T., Liu, J., Li, H., Xu, Y., Gu, W., Shen, L., 2019. Numerical and experimental investigation of precast concrete façade integrated with solar photovoltaic panels. *Appl. Energy* 253. <https://doi.org/10.1016/j.apenergy.2019.113509>.
- Marion, B., Adelstein, J., Boyle, K., et al., 2005. Performance parameters for grid-connected PV systems. In: 31st IEEE photovoltaics specialists conference and exhibition proceedings. Florida, pp. 1601–1606.
- Muehleisen, W., Loeschig, J., Feichtner, M., Burgers, A.R., Bende, E.E., Zamini, S., Yerasimou, Y., Kosel, J., Hirschl, C., Georgiou, G.E., 2021. Energy yield measurement of an elevated PV system on a white flat roof and a performance comparison of monofacial and bifacial modules. *Renew. Energy* 170, 613–619.
- Peng, J., Lu, L., Yang, H., Han, J., 2013. Investigation on the annual thermal performance of a photovoltaic wall mounted on a multi-layer façade. *Appl. Energy* 112, 646–656.
- Raybaud, B., Thony, P., Vergnault, E., Merlier, L., Roux, J.-J., 2019. Preliminary Numerical Evaluation of the BIPV's Potential in Urban Areas: Which Method to Use for Solar Radiation Calculation? BS2019: 16th IBPSA Conference proceedings, Rome. ISBN: 978-1-7750520-1-2. ISSN: 2522-2708.
- Sanjuan, C., Sanchez, M.N., Heras, M.D.R., Blanco, E., 2011a. Experimental analysis of natural convection in open joint ventilated façades with 2D PIV. *Build. Environ.* 46, 2314–2325.
- Sanjuan, C., Suarez, M.J., Gonzalez, M., Pistono, J., Blanco, E., 2011b. Energy performance of an open-joint ventilated façade compared with a conventional sealed cavity façade. *Sol. Energy* 85, 1851–1863.
- Saretta, E., Caputo, P., Frontini, F., 2019. A review study about energy renovation of building facades with BIPV in urban environment. *Sustain. Cities Soc.* 44, 343–355.
- Shukla, A.K., Sudhakar, K., Baredar, P., 2017. Recent advancement in BIPV product technologies: A review. *Energy Build.* 140, 188–195.
- Soria, B., Gerritsen, E., Lefillastre, P., Broquin, J.-E., 2015. A study of the annual performance of bifacial photovoltaic modules in the case of vertical facade integration. <https://doi.org/10.1002/ese3.103>.
- Tina, G.M., Scavo, F.B., Aneli, S., 2020. A novel building ventilated façade with integrated bifacial photovoltaic modules: analysis of the electrical and thermal performances. In: 5th International Conference on Smart and Sustainable Technologies (SpliTech). <https://doi.org/10.23919/SpliTech49282.2020.9243810>.
- Vulkan, A., Dorman, M., Errell, E., 2018. Modeling the potential for PV installation in residential buildings in dense urban areas. *Energy Build.* 169, 97–109.
- Wang, M., Peng, J., Li, N., Yang, H., Wang, C., Li, X., et al., 2017. Comparison of energy performance between PV double skin facades and PV insulating glass units. *Appl. Energy* 194, 148–160.
- Yu, G., Yang, H., Yan, Z., Ansah, M.K., 2021. A review of designs and performance of façade-based building integrated photovoltaic-thermal (BIPVT) systems. *Appl. Therm. Eng.* 182 <https://doi.org/10.1016/j.applthermaleng.2020.116081>.